Rapid Thermal Modeling of Wire Arc Additive Manufacturing Process using a Mesh-free Spectral Graph Theory Approach

Nicholas L. Piercy[a], Janmejay D. Kulkarni[b], Aramuriparambil Santhosh Vishnu[b], Simhambhatla Suryakumar[b], Kevin D. Cole[a*], Prahalada Rao[c]

[*]Corresponding Author (kcole1@unl.edu)
[a]Mechanical and Materials Engineering, University of Nebraska-Lincoln, Nebraska, USA
[b]Mechanical Engineering, Indian Institute of Technology-Hyderabad, Telangana, India
[c]Grado Department of Industrial and Systems Engineering, Virginia Tech, Virginia, USA

Abstract

The objective of this paper is to develop, verify, and experimentally validate a mesh-free spectral graph theory-based approach for rapid prediction of thermal history in metal parts made using the wire arc additive manufacturing (WAAM) process. Accurate and rapid prediction of the thermal history is a critical prerequisite for functional quality assurance of WAAM parts. In the spectral graph method, the WAAM part is represented as a set of discrete nodes encompassed by a network graph. The thermal history is obtained by solving the heat equation on the network graph. The spectral graph theory approach thus bypasses the cumbersome computational burden associated with mesh generation in the finite element method. To validate the spectral graph theory approach, experimental temperature data is acquired for multi-layer mild steel WAAM parts processed under six different combinations of shape and inter-layer dwell time conditions. Further, each experiment was replicated resulting in a total of 12 parts. The accuracy of the thermal trends predicted by the spectral graph theory approach was quantified in terms of the symmetric mean absolute percent error (SMAPE) and root mean squared error (RMSE, °C). The thermal history trends were predicted with SMAPE < 5% and RMSE < 11 °C relative to the experimental temperature measurements. The computation time to obtain the thermal history of each 21-layer part was approximately 3.5 to 4 hours. The spectral graph theory predictions were further verified with a commercial finite element software package (Simufact-Welding). For a similar level of SMAPE and RMSE as the spectral graph theory approach, the FE-based Simufact predictions required over 7.5 hours. The computational advantage of the spectral graph theory approach is particularly valuable for devising physics-based process parameter optimization and feedforward control strategies to mitigate flaw formation in WAAM parts.

Keywords: Wire and arc directed energy deposition, computational thermal modeling, spectral graph theory, thermal history.

1. Introduction

1.1 Background, Objective and Rationale

In the wire arc additive manufacturing (WAAM) process, material feedstock in the form of wire is fused layer-by-layer using an electric arc to create 3D freeform geometry metal parts. The geometrical freedom of the WAAM process is enabled by the relative motion between the substrate and the welding torch, which can be achieved either by a multi-axis machine tool or a robotic arm [1]. The process belongs to the wire and arc directed energy deposition (WA-DED) family of additive manufacturing (AM) processes and is based on gas metal arc welding [2].

A schematic of the WAAM process is shown in Figure 1, where the energy from the electric arc melts the wire feedstock and the arc is surrounded by a shielding gas, typically argon or a mixture of argon and carbon dioxide, which prevents oxidation and contamination of the meltpool, as well as protects and stabilizes the arc. Popular materials for WAAM include non-ferrous metals, such as aluminum and titanium, as well as ferrous alloys, such as stainless steel and mild steel (this work).

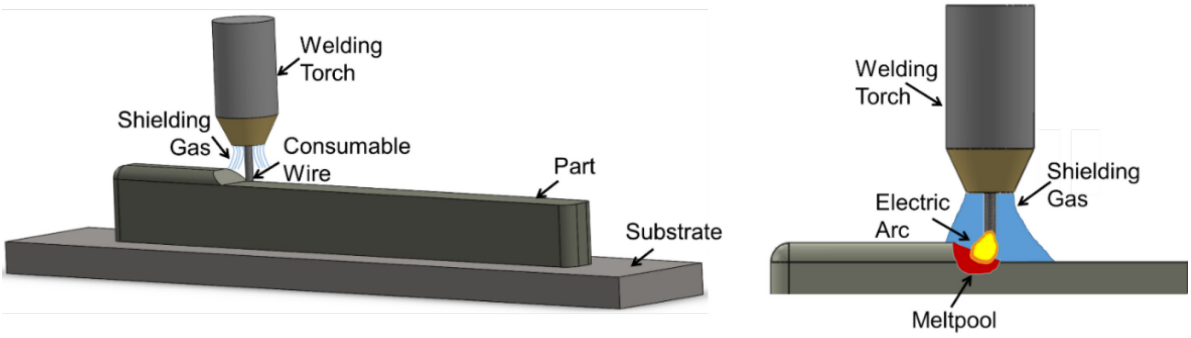

Figure 1: Schematic of the wire arc additive manufacturing (WAAM) process. A welding head deposits material via the use of a consumable electrode which is melted with an electric arc struck between the part and electrode.

The primary advantage of WAAM, in comparison to powder-based AM processes such as powder-based DED (P-DED) and laser powder bed fusion (LPBF), is its cost-effectiveness, high deposition rates, large material utilization, and scalability to large volume manufacturing [3]. Holshouser et al. [4] discuss the scalability of WAAM by introducing the field of big area additive manufacturing (BAAM), which features an essentially unlimited build chamber supported by the fast deposition speeds in WAAM. While commercial P-DED systems typically deposit material at a rate near 0.5 kg per hour, the high deposition rates in WAAM deliver over 5 kg per hour [5].

The objective of this paper is to develop, verify, and experimentally validate a spectral graph theory-based approach for rapid prediction of the spatiotemporal temperature distribution (thermal history) in WAAM parts during the printing process. This is an important area of research, because, despite its demonstrated capabilities, WAAM parts suffer from flaws such as distortion in shape and poor surface finish due to regional retention of heat (overheating) and uneven cooling [6]. The high deposition rates of WAAM are accompanied by high energy input. As demonstrated in a study by Jin et al. [7] the energy input during WAAM processing of stainless steel 316 is 5-10 times greater than that of laser-based additive manufacturing processes.

As build height increases, heat dissipation through conduction to the previously deposited material slows, leading to heat accumulation [8]. Furthermore, the cyclical heating and cooling of the part, on account of the layer-by-layer nature of the process, leads to inconsistencies in the microstructure and consequently undermines the functional properties of the part [9]. Heating and cooling rates are governed by the part thermal history [10]. The thermal history is a function of the part shape, material properties, and process parameters, such as the welding energy (voltage and current), path translated by the welding torch to deposit material (tool path), deposition velocity, wire feed rate, and interlayer dwell time, among others.

Hence, in the context of WAAM, as shown in Figure 2, an accurate and rapid thermal model is the key to physics-based process optimization, feed-forward control, and predicting the impact of many possible combinations of processing parameters on microstructure evolved and mechanical properties [11]. To address these needs, this work advances a computational approach to predict the thermal history in WAAM parts based on the theory of heat diffusion on graphs (spectral graph theory). Using the spectral graph approach, practitioners can rapidly predict the thermal history for a WAAM component as a function of key process variables, such as welding power, tool path, and interlayer dwell time. Based on the insights obtained from these thermal simulations, the processing conditions can be optimized to avoid flaw formation, such as overheating before printing the part – a form of feedforward control. As shown in recent publications with other AM processes, the cooling rate derived from the thermal history simulations can be further leveraged to estimate microstructure aspects, e.g., grain size and meltpool depth, and mechanical properties [12, 13].

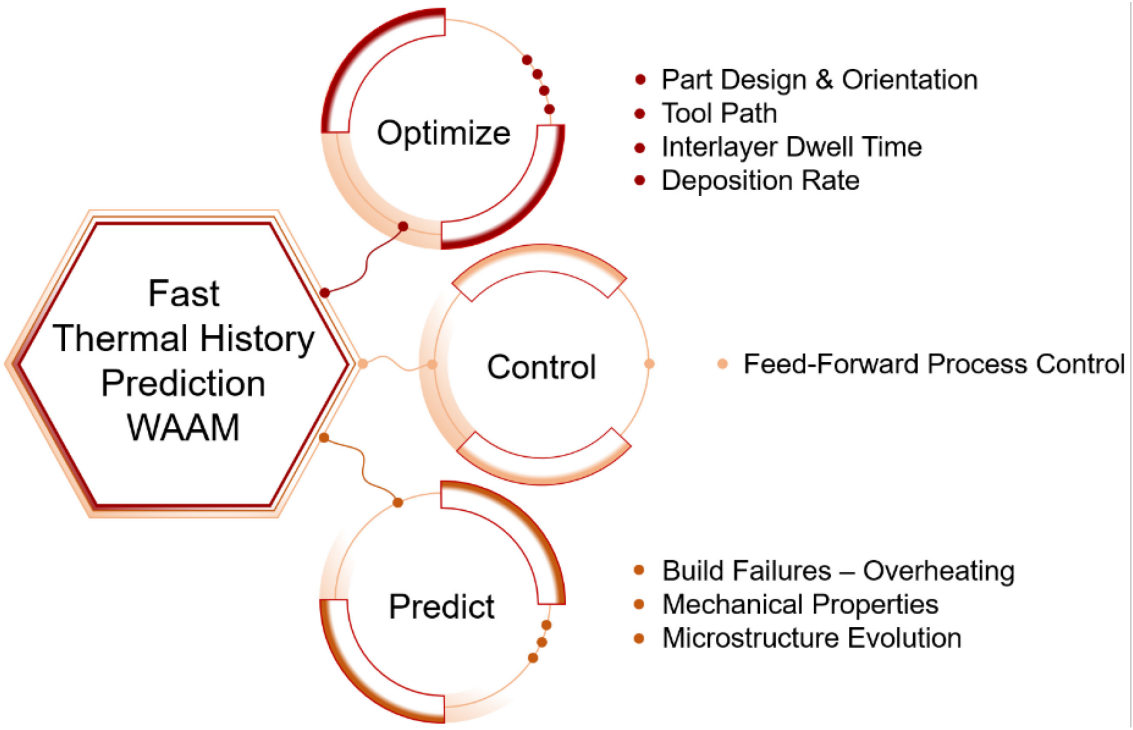

Figure 2: Fast and accurate modeling of thermal history is central to quality assurance in WAAM.

1.2 Literature Review – Prior Work and Novelty

1.2.1 Finite Element-based and Other Approaches for Thermal Modeling in AM

Thermal history simulation of AM processes is typically performed using both commercially available and proprietary finite element (FE) software [14]. A major drawback of using FE-based methods is the long simulation time, often requiring many hours, if not days, to converge, which becomes progressively worse with part size [15].

An inherent obstacle in thermal simulation of AM processes, including WAAM, is the increase of mass as material is incrementally added. In other words, the computational domain in FE-based simulation of the AM processes evolves continually, which requires repeated re-meshing – a computationally cumbersome activity [16]. Consequently, meshing solutions, such as the quiet-element method (element birth method) and the inactive-element method have been introduced to overcome the computational burden associated with meshing in AM [17]. In the literature, many unique whole-part thermal modeling approaches have been used to improve computation time without significant loss of accuracy for thermal history simulation of LPBF and DED processes. Herewith we summarize representative papers from the literature.

In the context of the LPBF process, Peng et al. [18] reported fast thermal simulations of builds using thermal circuit elements (TCE) which are thermal masses connected by thermal resistors. Compared to a conventional FE simulation of a realistic part using 16000 nodes, 40 thermal circuit elements give temperatures two orders of magnitude faster with errors less than 15%. Likewise, Tangestani et al. [19] sped up FE simulations for temperature by integrating the 3D gaussian heating function over time and applying it along the line of laser motion. In a 2 mm × 1 mm × 0.5 mm LPBF geometry, this approach provided temperature simulation 330 times faster than traditional FE with errors less than 15%.

Dugast et al. [20] carried out fast thermal simulations of the LPBF process by porting code to a graphics processing unit (GPU). When applied to the build of a 25 mm cube, the temperature simulation was 300 times faster with error less than 1% compared with a commercial FE simulation. Mozaffar et al. [21] implemented a GPU-based strategy for FE simulations of metal additive manufacturing processes and reported convergence exceeding 100× faster than an optimized single core CPU.

For the DED process, a common theme in the literature is that computational improvement involved changing the way heat is added to the model. Stockman et al. [22] describe a coarse-mesh finite-difference model used to simulate temperatures in a DED process with simplified heat input of a specified melt temperature for the added material. Simulation of a rectangular wall consisting of 31 layers of two side-by-side passes with final size about 76 mm high, 127 mm long, and 7 mm wide was carried out with 77,000 nodes, which ran in 12 minutes on a single CPU laptop. No comparison of processing time was made with conventional FE methods, however temperature values tracked well with experimental thermocouple data from a DED build.

Ding et al. [23] provided faster temperature simulations for the WAAM process by replacing Gaussian heating by well-distributed volumetric heating in each added mass element. In an FE simulation (Ansys) of a block-shaped part with 10 layers, each of size 150 mm × 30 mm with 5 zig-zag hatches per layer, the well-distributed heating model was 17 times faster with errors within 6%. Temperature results were also compared with experimental data.

Nijhuis et al. [24] provided faster simulated temperatures in the WAAM process by holding newly deposited mass elements at an elevated temperature for a dwell time t_d, after which the newly added mass is allowed to cool by diffusion. In simulating a thin wall 1 mm wide, 10-layers tall, and 12 mm long, the method was 4.3 times faster, with comparable

precision, than a conventional FE simulation with a volumetric moving heat source. Yang et al. [25] employed a semi-analytical model for the WAAM process by superposing point-source infinite-space solutions with a complementary correction temperature field, provided by a coarse-grid FE calculation, to enforce thermal boundary conditions in the finite body. When applied to a thin wall geometry 2 mm wide × 4 layers tall × 500 mm long, the method provided temperature values 2 times faster than a conventional FE simulation with errors less than 10%.

Kovšca et al. [26] developed a boundary detection method which was used in conjunction with the inactive element FE approach to assign local boundary heat loss parameters simultaneously within the element activation routine. This technique was used for modeling of thermal history in a 10-layer cylindrical WAAM thin-wall measuring 15 mm tall, 52 mm in diameter, and 4.2 mm in wall thickness. Though the computation time is not reported, the simulated temperatures trend with the experimental data, with increasing agreement toward the end of each interlayer dwell period.

Several cases from the literature are reported in Table 1 to demonstrate the computation times associated with FE-based thermal simulations for WAAM. The representative cases were chosen such that the volume of material deposited was similar to that of the parts studied in this work (~ 12.7 to 13×10^4 mm^3). Specifically, Ding et al. [27] simulated a four-layer thin-wall which had a single weld pass per layer. Graf et al. [28] simulated a 46-layer cylindrical tube which consists of single weld tracks per layer. Ahmad et al. [29] simulated a five-layer wall consisting of three weld tracks per layer. These simulations utilized the element birth technique and typically used a coarse mesh to simulate the substrate. The approximate simulated volumes reported in Table 1 account for the printed geometry as well as the substrate.

Table 1: Computational times reported by various researchers using finite element models for thermal history prediction in WAAM.

Authors	Component simulated	Approximate volume simulated [mm^3]	System specifications	Approximate computation time
Ding et al. [27]	4-layer rectangular thin-wall	38×10^4	Grid computing with 4 processors	51 hrs 24 min
Graf et al. [28]	46-layer cylindrical thin-wall tube	7.8×10^4	12 core processors	82 hrs
Ahmad et al. [29]	5-layer, 3-pass rectangular wall	18×10^4	Not Available	35 hrs

1.2.2 Spectral Graph Theory-based Thermal Modeling of Additive Manufacturing

To overcome the challenges with FE-based thermal modeling in AM, Yavari et al. [30] developed a mesh-free spectral graph theory-based thermal model for applications in LPBF. In the spectral graph method, a 3D geometry is represented by a cloud of discrete nodes and the heat equation is solved over these nodes. Their work was verified against FE models, where the verification process encompassed custom code implemented in ABAQUS, as well as commercial software (Netfabb). Yavari et al. [31] further provided validation using in-process infrared thermal camera-derived surface temperatures, which were obtained for a range of simple prismatic shapes as well as complex practical objects, such as a 125 mm × 25 mm impeller. They report that spectral graph theory thermal simulations for LPBF parts converged 3 to 5 times faster than FE models with the same level of prediction error with respect to experimentally observed temperature measurements.

Riensche et al. [32] previously applied a spectral graph theory approach to thin-wall P-DED parts which converged substantially faster than FE. Though the prior work involved P-DED, the treatment of heat input from the welding source as well as boundary heat loss were similar to the approach developed for LPBF. For example, the heat input was modeled as an instantaneous temperature rise with subsequent heat conduction occurring throughout the part. Also, the boundaries were assumed to be insulated, with heat loss occurring as a temperature

amendment to the boundary nodes outside of the spectral graph method. These assumptions align with the LPBF process where the layer-wise heating is considerably faster, and the powder bed serves to insulate the part during processing. However, the foregoing assumptions are not applicable to the WAAM process. As shown in Figure 3, heat transfer in WAAM is comprised of conduction within the part, heat loss to the surroundings due to radiation, free convection due to the thermal interaction between the part and the surroundings, and forced convection due to continuous, localized shielding-gas flow.

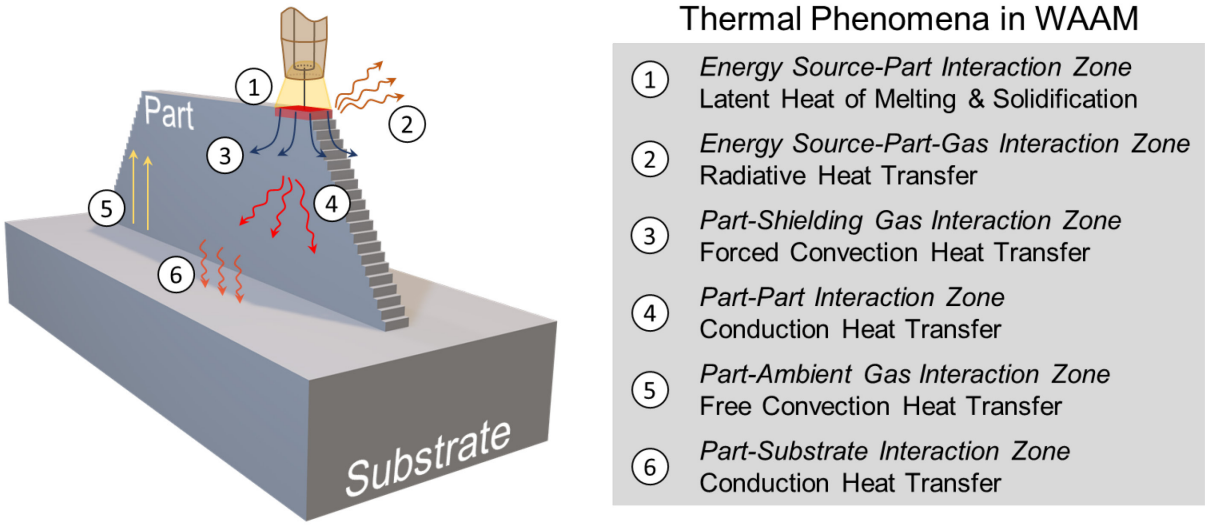

Figure 3: Thermal phenomena in WAAM: (1) Heat input from the welding source; (2) Radiation to the surrounding gas; (3) Forced convection due to the flow of shielding gas; (4) Conduction within the part; (5) Free convection with the surrounding gas; and (6) Conduction between the part and substrate.

In recent work, Cole et al. [33] extended the theoretical foundations of the spectral graph theory approach through discrete Green's function analysis and compared the results for benchmark heat transfer problems (1D and 3D cases) with respect to analytical, finite difference, and finite element methods. These theoretical studies affirmed the computational advantages of the spectral graph theory approach and provides volumetric heating and boundary heat loss as an integral part of the spectral graph method.

In the present work, the advances of Cole et al. [33] are applied toward modeling of the thermal history of parts produced using the WAAM process. Although the conceptual

underpinnings of this work are motivated from the authors' prior work in the context of P-DED, the physics-based enhancements presented in this paper permit a more careful consideration of the thermal phenomenon unique to the WAAM process. The enhancements to the spectral graph approach described in this paper are best characterized by a physics-based representation of the local welding heat source using volumetric internal heat generation, and consideration of boundary heat loss occurring within the spectral graph method. While the consideration of boundary heat loss eliminates a second computational step by embedding boundary details within the Laplacian matrix, volumetric internal heat generation incorporates processing parameters into the mathematical formulation of the heat equation.

The remainder of this paper is organized as follows. In Section 2, the details of the experiments are summarized, and the obtained thermal data is presented. Section 3 explains the development of the spectral graph method for modeling thermal history in WAAM. Section 4 verifies and validates the spectral graph method by comparison between model derived thermal history predictions and commercial FE simulations, and thermal data obtained from experiments, respectively. Finally, Section 5 concludes the work and provides an outlook for future research.

2. Experiments

Six controlled experiments were conducted in this work, each with one replicate to account for measurement variability. The experiments used one of two different part geometries along with various interlayer dwell times – that is the time which elapses between the end of deposition for one layer and the start of deposition of the subsequent layer. The rationale for these experiments is as follows. As mentioned in Section 1, in WAAM the thermal history is a function of process parameters, material characteristics, and part shape. Thus, in accordance with the goal of this work, the experiments are designed to ascertain the ability of the model to capture various thermal histories resulting from change in the part geometry, as well as an important processing parameter (interlayer dwell time).

2.1 Experimental Setup

The WAAM setup consists of a 3-axis CNC machine tool (Bharat Fritz Werner, model Agni BMV 45 TC20). The vertical (z) axis of the machine is coupled to a cold metal transfer (CMT) welding torch (Fronius Transpuls Synergic) as embodied in Figure 4(a) and (b).

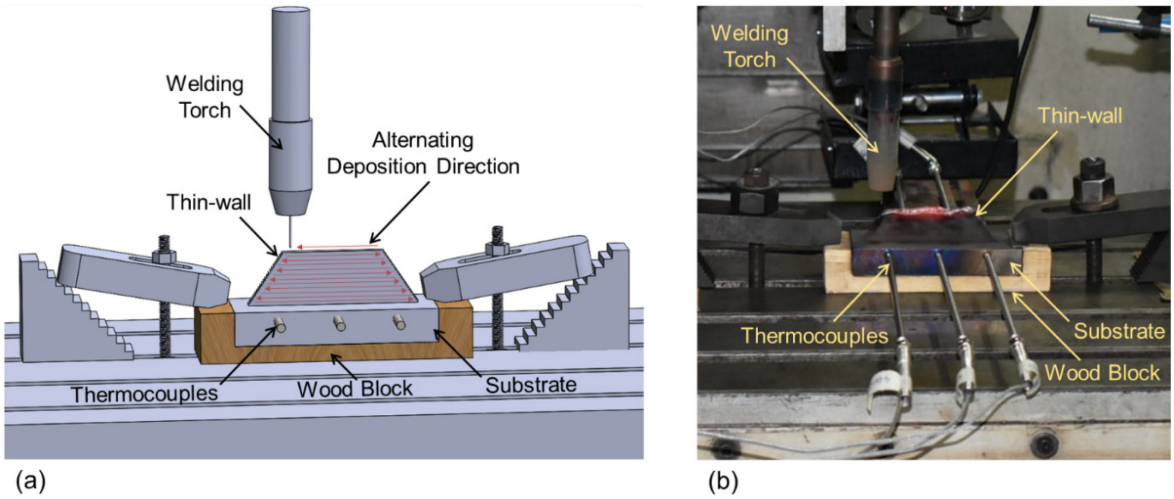

Figure 4: Experimental setup for the deposition of thin-walls, (a) schematic of experimental setup, (b) actual setup during weld deposition of a trapezoid thin-wall.

A mild steel (EN8) substrate measuring 120 mm × 48 mm × 20 mm is used in this work. The feedstock is mild steel wire (ER70S-6, C 0.06 - 0.15 wt. %). The substrate was fixed to a C-shaped wooden block (for thermal isolation), as shown in Figure 5(c). The substrate and wooden block were subsequently clamped to the bed of the machine tool. Five equidistant blind holes were drilled 25 mm deep into the substrate at a distance of 15 mm from the bottom surface. Temperature data are acquired by installing five sheathed, ungrounded, K-type (Cr/Al) thermocouples (5 mm diameter × 200 mm long) in the substrate within these blind holes. A thermal compound was introduced in the blind holes to ensure (thermal) coupling of the thermocouple probes to the substrate. A National Instruments data acquisition system (NI-9212) was used for continuous logging of temperature data at a sampling rate of 2 Hz.

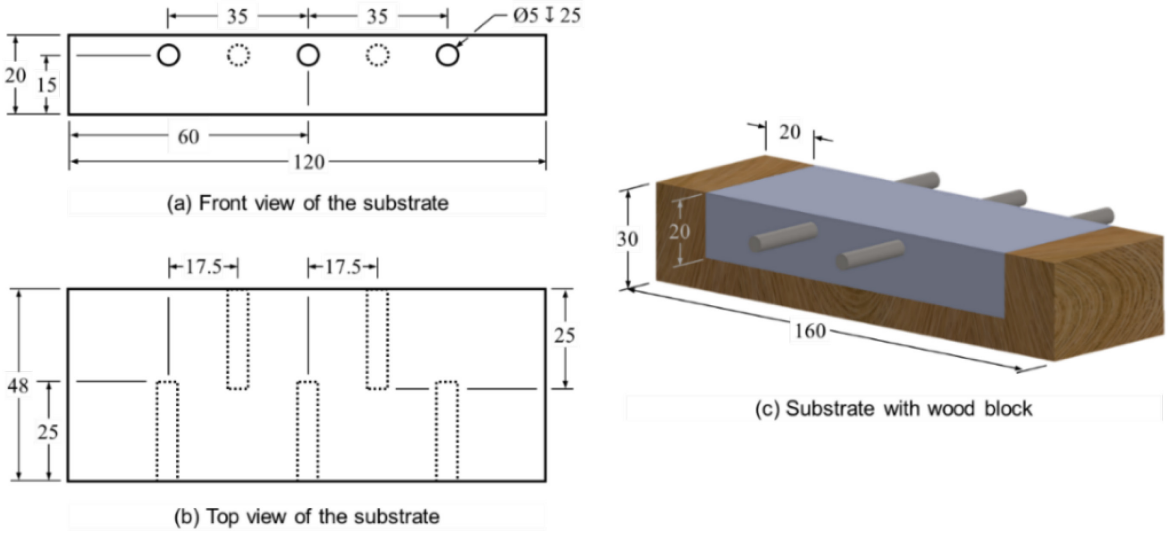

Figure 5: Substrate and thermocouple locations given in [mm], (a) Front view of the substrate, (b) Top view of the substrate, (c) Substrate with the wooden block.

While a higher sampling rate would be valuable for capturing rapid temperature fluctuations and predicting instantaneous temperature closer to the deposited layer, however, the focus of this work is in predicting part-scale temperature deviations which occur at a much slower rate, the sampling rate of 2 Hz would be adequate. Indeed, 5 thermocouples have been placed in the substrate, which implies we acquire thermal data every 1.3 mm of deposition. As the first layer is deposited, each thermocouple is centered 5 mm in depth farther from the

deposition zone, and successive layers are deposited at larger and larger distances from the thermocouples. Thermal diffusion through 5 mm or more of metal would attenuate the sharp temperature peaks near the deposition zone, such rounded peaks are observed in the thermocouple data discussed later in the context of Figure 9 – Figure 11.

While attempts have been made to use infrared (IR) thermal imaging to capture temperature distribution in the part, the measurements reported by IR thermal cameras are relative trends and not absolute temperature measurements [34]. This is because the energy radiated by a surface, which is converted to a temperature reading by an IR thermal camera, is dependent on the emissivity of the material. The material emissivity is not a constant value but depends on the surface roughness and temperature of the body, among other factors. Furthermore, the angle of inclination between the thermal camera and the surface also has an effect. Hence, calibration of an IR thermal camera to provide absolute temperature readings is a particularly challenging proposition in WAAM. Hence, to eschew these pitfalls, we used contact thermocouples embedded within the substrate. Lastly, as the focus this work is on modeling part-scale thermal history, measurements of meltpool temperatures using a pyrometer were not conducted. In our future work, we will endeavor to correlate the part-scale temperature with the microstructure evolved.

Researchers have also welded thermocouples to the part to obtain near-instantaneous layer-level temperature [26]. While in this work thermocouples have not been welded to the part to avoid inconsistencies in the inter-layer dwell time, we have verified the thermal history predictions at both the part- and the layer-levels with a commercial finite element package (Simufact Additive).

2.2 Processing Conditions and Build Plan

Two rectangular and four trapezoidal shaped experimental thin-wall parts were manufactured, each with a specified interlayer dwell time, for a total of six experiments. While six experiments were studied, each experiment was replicated once to consider variation between builds, which resulted in a total of 12 thin-walls being manufactured. The rectangular and trapezoidal part geometries are shown in Figure 6. Regardless of the interlayer dwell time, a total of 21 deposition layers were required to manufacture both the rectangular and trapezoidal thin-walls, where a single hatch (weld track/bead) was deposited per layer in an alternating to-and-fro hatch pattern, as shown in Figure 4(a) and Figure 6(b). The length of each layer in the rectangular walls was 100 mm. For the trapezoidal walls, the first layer was of length 100 mm and each layer thereafter decreased in total length by 2mm (1 mm reduction from each end), resulting in a layer length of 60 mm for the final (21st) layer. All experimental parts measure 31.5 mm in height and 4.7 mm in width. Each hatch is 4.7 mm in width and 1.5 mm in height. The arc voltage (14.8 VDC) and current (110 A) are maintained constant for all experiments along with other parameters shown in Table 2.

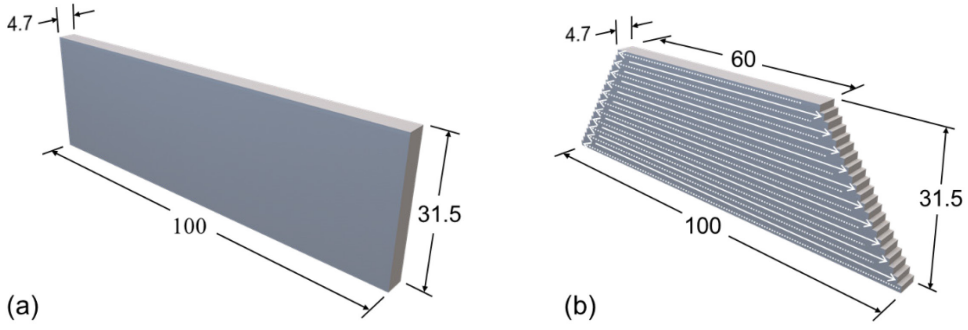

Figure 6: Experimental component geometries without substrate, shown with dimensions [mm], (a) rectangle part, (b) trapezoid part. The arrows overlayed on the trapezoid part show the tool path, where the layers are deposited in a to-and-fro fashion.

These processing parameters were optimized in prior work by Panchagnula and Simhambhatla so as to avoid flaw formation and provide an acceptable quality build [35]. The elapsed time between deposition of subsequent layers, known as the interlayer dwell time (t_d)

was varied between experiments. The interlayer dwell time is an important factor because it influences the initial thermal field present prior to deposition. To explain further, the initial thermal field prior to deposition influences the cooling and solidification rates, which in turn governs the microstructure morphology and thermal-induced residual stress [36]. For example, an elevated initial thermal field prior to deposition acts similarly to pre-heating the previously deposited and solidified layers, which impacts the depth of re-melting in the previous layers, and directly affects microstructure evolved [37]. In our future work, we will endeavor to study the effect of welding power, velocity, and toolpath from the perspective of feedforward process control. We note that, since the difference between the rectangular and trapezoidal part geometries lies in the length of each layer, the interlayer dwell time is chosen to vary as a function of the time required to deposit either the first layer or the previously deposited layer of each geometry and is described below.

Considering the rectangle geometry shown in Figure 6(a), having uniform hatch lengths $l = 100$ mm and a weld torch velocity $v = 11.67\ \text{mm} \cdot \text{s}^{-1}$, the time to deposit the first layer, as well as all subsequent layers, is $t_1 \approx 8.57$ seconds. Since the layer-wise length remains constant for the rectangle geometry, the calculated interlayer dwell time using either the first-layer or the previous-layer approach results in the same interlayer dwell time. Accordingly, the two rectangular thin-wall parts, termed *Rect43* and *Rect86*, were built with the following interlayer dwell times (t_d):

- *Rect43*, $t_d = 5 \times t_1 \approx 43$ seconds, i.e., 5 times the deposition time for the first layer t_1.
- *Rect86*, $t_d = 10 \times t_1 \approx 86$ seconds, i.e., 10 times the deposition time for the first layer t_1.

Likewise, the four trapezoidal thin-wall parts, termed *Trap43, Trap86, Trap5×, Trap10×*, were built with the following interlayer dwell times (t_d):

- *Trap43*, $t_d = 5 \times t_1 \approx 43$ seconds, i.e., 5 times the deposition time for the first layer t_1.

- *Trap86*, $t_d = 10 \times t_1 \approx 86$ seconds, i.e., 10 times the deposition time for the first layer t_1.
- *Trap5×*, $t_d = 5 \times t_{i-1}$, where t_{i-1} is the deposition time for the previous layer, i.e., 5 times the deposition time required for the previous layer.
- *Trap10×*, $t_d = 10 \times t_{i-1}$, where t_{i-1} is the deposition time for the previous layer, i.e., 10 times the deposition time required for the previous layer.

While *Rect43, Rect86, Trap43,* and *Trap86* are built with a constant interlayer dwell time of either 43 or 86 seconds, *Trap5×* and *Trap10×* are built with a dynamic interlayer dwell time that progressively decreases due to the layer-by-layer reduction of layer length, reducing the time required to deposit each subsequent layer. The layer-wise interlayer dwell times for all experiments are depicted in Figure 7. These dwell times were selected based on extensive trials not reported in this work.

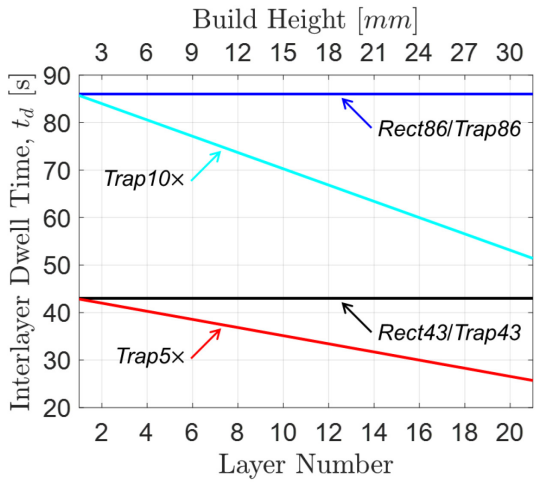

Figure 7: Interlayer dwell time vs. layer number and build height. Cases *Trap5×* and *Trap10×* have decreasing interlayer dwell times due to the progressive reduction in layer length.

Table 2: Processing parameters that are held constant throughout all experiments.

Current (I)	110 A
Voltage (V)	14.8 VDC
Wire diameter (d)	0.8 mm
Wire feed rate (w_f)	9.8 m·min^{-1} (163.3 mm·sec^{-1})
Torch speed (v)	0.7 m·min^{-1} (11.67 mm·sec^{-1})
Shielding gas	82 % Ar + 18% CO2
Gas flow rate	7.5 L·min^{-1}

2.3 Temperature Data Acquisition

The data obtained from the thermocouples is reported in the form of temperature vs. time plots. The thermocouples are labeled TC1 through TC5, contingent on their location with respect to the substrate, as shown in Figure 8. The thermocouples installed in the front of the substrate are labelled as TC1, TC3, and TC5; the thermocouples installed in the back of the substrate are labelled TC2 and TC4. Upon examination of the data, TC5 provided incoherent temperature trends, hence it is not used in this work.

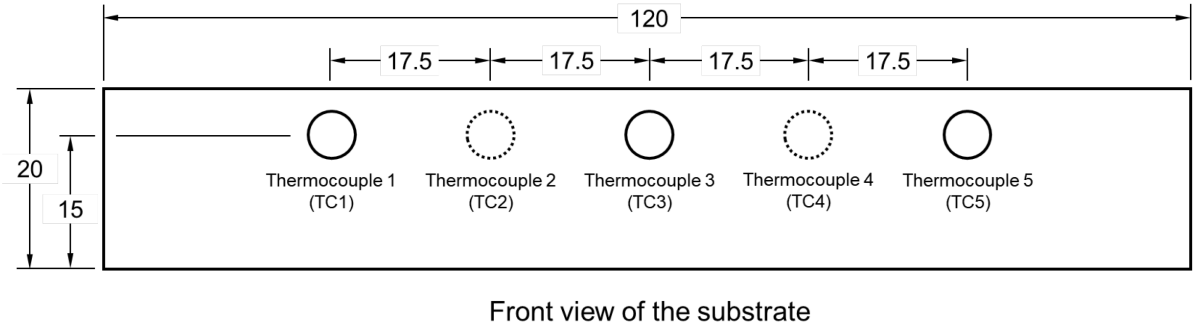

Figure 8: Names of thermocouples and their location within the substrate. Dimensions shown are [mm].

Figure 9(a) and (b) show the temperature trends recorded by thermocouples TC1, TC2, TC3, and TC4 for one replication of the *Rect43* and *Rect86* cases, respectively. Consider Figure 9(a), which shows thermocouple data for the *Rect43* rectangular thin-wall with 43 second interlayer dwell time. The total build duration is roughly 1100 seconds (~ 18.5 minutes). The data has 21 periodic peaks, corresponding to the 21 passes (layers) of the torch. Early in the build, each pass of the torch causes a steep rise in temperature followed by rapid temperature decay. Later, as the part grows in height and the build plane moves away from the thermocouples, each pass of the welding torch produces a smaller temperature rise in the substrate, hence each peak is less pronounced. Referring to Figure 9, we note that although the temperature peaks may appear to occur at the same time in the plots, they are offset slightly due to their physical position in the substrate. For example, for the rectangular cases, the time to deposit each layer is 8.57 s which means that all the thermocouples are subjected to a heated

environment during that time. Hence, the individual thermocouple responses will be slightly offset from each other, but they will appear in groups with similar behavior since each group of peaks corresponds to a single layer being deposited.

In Figure 9 there is some variation in the magnitude of the temperature peaks among the different thermocouple locations. These temperature magnitude differences may be explained as an effect of the heat flow from the center of the substrate towards the cooler ends of the substrate where no part is being built and where no heat is being added. The measurements from TC 3 are highest as it is located at the centerline of the substrate. Slightly lower temperature peaks are observed for TC 2 and TC 4, which are at located 17.5 mm from the centerline. The lowest temperature peaks are observed from TC 1 which is located 35 mm from the centerline.

The following is evidence that the fixed data rate of 2 Hz is adequate for capturing the shape of the temperature peaks at the thermocouple locations. In comparing Figure 9 (a) and (b), we note that the duration of the Rect86 experiment was two times longer than the Rect43 experiment. Although rise time of the temperature peaks early in the build in Figure 9 (b) may appear to be steeper than those in Figure 9 (a), they are of equal steepness when the rise time is accounted. Further, the temperature peaks depicted in Figure 9 (a) and Figure 9 (b) have comparable heights, even though the two experiments are of different duration (Figure 9 (b)) is two times longer and contains twice as many data points compared to Figure 9(a)).

The temperature trends in Figure 9 can be further explained by heat flow in and heat flow out. For the rectangular thin-wall, each successive layer is of the same dimension. Hence, the energy per deposited layer remains constant throughout the build. However, as the build grows in height, the increased surface area of the part accelerates heat loss due to radiation and convection (forced and free convection – more surface area is exposed to the shielding gas). A similar trend is observed in Figure 9(b) for the *Rect86* thin-wall part with 86 second interlayer

dwell time between layer deposition. The build duration for the *Rect86* thin-wall part is 2000 seconds (~ 33.5 minutes).

Shown in Figure 10(a) and (b) are the temperature trends for the trapezoid-shaped thin-wall parts with constant interlayer dwell times of 43 seconds (*Trap43)* and 86 seconds (*Trap86)*, respectively. The total build duration is 1050 seconds (~ 17.5 minutes) and 1950 seconds (~ 32.5 minutes) for cases *Trap43* and *Trap86*, respectively. These trapezoidal thin-walls depict a lower temperature trend in comparison to their rectangular counterparts, because successively deposited layers in the trapezoid shape are smaller, resulting in successively less material deposition and heat input.

Figure 11(a) and (b) show the temperature trends for the trapezoid-shaped thin-wall parts *Trap5*× and *Trap10*×, built with varying interlayer dwell time, where the interlayer dwell times are shown in Figure 7. The total build duration is 870 seconds (~ 14.5 minutes) and 1590 seconds (~ 26.5 minutes) for cases *Trap5*× and *Trap10*×, respectively.

Among the rectangle-shape cases, the maximum temperature experienced by any thermocouple is near 275 °C for case *Rect43*, and 225 °C for case *Rect86*. Amongst the cases *Trap43* and *Trap86*, i.e., for the trapezoid walls with constant dwell time, the temperature curves flatten out toward the end of the build. For the longer dwell times, some temperature curves begin to fall after reaching a maximum value. Similar trends are observed for cases *Trap5*× and *Trap10*×. These observations may be explained by the lower heat input for the trapezoidal geometries compared to the rectangular geometries, and by the additional time for cooling when the dwell time is longer.

Since each thin-wall was built twice, the variation between experiments can be quantified in terms of the root mean square (RMS) deviation. The RMS deviation for a majority of the

cases is within 15 °C, with a maximum of 17 °C, and a minimum of 3 °C. The RMS deviation between experiments for each thin-wall is reported in Appendix A

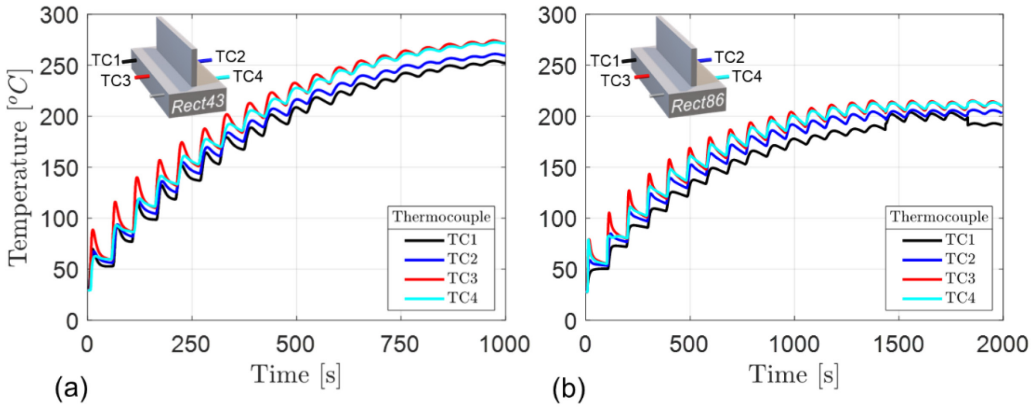

Figure 9: Recorded temperature trends by four thermocouples (TC1, 2, 3, 4) for: (a) *Rect43* rectangular thin-wall with a constant 43 second interlayer dwell time ($t_d = 43$ s), and (b) *Rect86* rectangular thin-wall with a constant 86 second interlayer dwell time ($t_d = 86$ s).

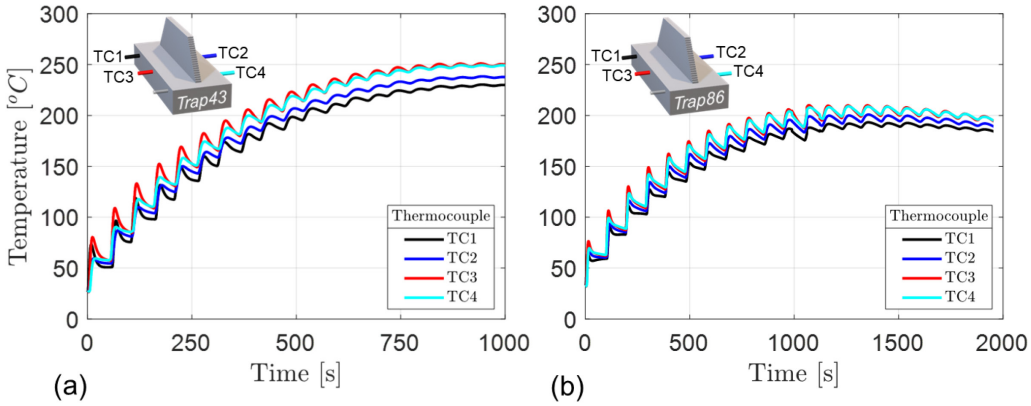

Figure 10: Temperature trends recorded by four thermocouples (TC1, 2, 3, 4) for: (a) *Trap43* trapezoidal thin-wall with a constant 43 second interlayer dwell time ($t_d = 43$ s), and (b) *Trap86* trapezoidal thin-wall with a constant 86 second interlayer dwell time ($t_d = 86$ s).

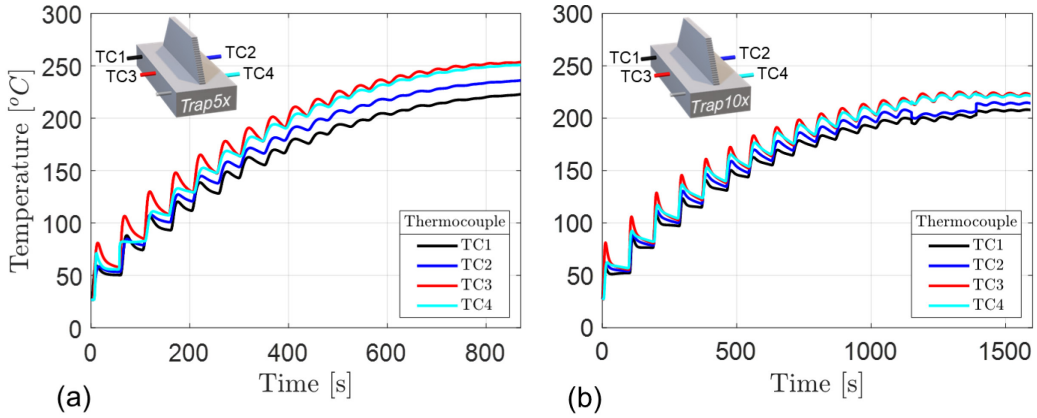

Figure 11: Temperature trends recorded by four thermocouples (TC1, 2, 3, 4) for: (a) *Trap5*× trapezoidal thin-wall with a non-constant interlayer dwell time equal to 5 times the deposition time of the previous layer ($t_d = 5 \times t_{i-1}$), and (b) *Trap10*× trapezoidal thin-wall with a non-constant interlayer dwell time equal to 10 times the deposition time of the previous layer ($t_d = 10 \times t_{i-1}$).

3. The Spectral Graph Method

3.1 Mathematical Foundations

Detailed works by Yavari et al. [30, 31] and Riensche et al. [38] discuss the graph theory solution with applications for LPBF, where heat from the fast-moving laser is modeled as an initial temperature condition in the heat equation for each layer. Due to the slow-moving heat source in WAAM, heat provided by the welding torch is instead represented by a volumetric heat source term. The heat equation to be solved, along with boundary and initial conditions, is given as:

$$\frac{1}{\alpha}\frac{\partial T}{\partial t} = \nabla^2 T + \frac{1}{k} g(r) \tag{1}$$

$$k\frac{\partial T}{\partial n} = h_{eff}(T_\infty - T) \qquad \text{(boundary condition)} \tag{2}$$

$$T(r, t = 0) = T_0(r) \qquad \text{(initial condition)} \tag{3}$$

where α $[\mathrm{m}^2 \cdot \mathrm{s}^{-1}]$ is the thermal diffusivity of the material, ∇^2 is the continuous Laplacian operator, k $[\mathrm{W} \cdot \mathrm{m}^{-1} \cdot \mathrm{K}^{-1}]$ is the thermal conductivity of the material, $g(r)$ $[\mathrm{W} \cdot \mathrm{m}^{-3}]$ is the heat source term which is a function of position, n represents the outward normal vector used for type 3 (convection) boundaries, h_{eff} $[\mathrm{W} \cdot \mathrm{m}^{-2} \cdot \mathrm{K}^{-1}]$ is an effective heat loss coefficient, and T_∞ [K] is the ambient temperature. An underlying assumption in the graph theory method is that Eqn. (1) is linear, requiring thermal properties (e.g., thermal diffusivity and conductivity) to be held constant. Recent work by Cole et al. [33] discusses the spectral graph method for solving the linear heat equation with a heat source term.

To address the actual temperature-dependent thermal properties present in the WAAM process, material properties, such as thermal diffusivity, are averaged over the range of expected temperatures. Since the graph theory approach is concerned with predicting temperatures over large ranges of dimensionless times and over the whole body, the effect of

non-uniform material properties is expected to be relatively smaller at the thermocouple locations. Nevertheless, we recognize the reasonable tradeoff in predictive precision vs. computation time resulting from maintaining fixed material properties.

In the graph theory method, the continuous Laplacian operator, ∇^2, which contains geometrical considerations for the part to be printed, is replaced with the discrete Laplacian matrix, L, and the continuous temperature is replaced by a discrete vector of temperatures at the node points in the domain. The Laplacian matrix ($N \times N$) is constructed from two matrices: the adjacency matrix ($A^{N\times N}$), and the diagonal degree matrix ($D^{N\times N}$).

The adjacency matrix, which is sparse, has entries a_{ij} called edge weights of the graph, i.e., $A = [a_{ij}]$ given by,

$$a_{ij} = \begin{cases} \dfrac{f}{d_{avg}^2} e^{\frac{(||c_i - c_j||^2 - d_{avg}^2)}{\sigma^2}} & ; \ ||c_i - c_j|| \le \varepsilon \\ 0 & ; \ ||c_i - c_j|| > \varepsilon \end{cases} \tag{4}$$

$$\varepsilon = \sqrt{2}\, d_{avg}$$

where ε is the neighbor radius, $||c_i - c_j||$ is the Euclidean distance between nodes i and j, and f is a calibration factor – a function of the node density. The factor (f) is found from a calibration procedure which is performed once for a given node density, then used for all simulations at that node density. The present rendition of the spectral graph method utilizes an edge weight formulation which relies on each node representing a uniform volume subset of the simulation domain, on average. In turn, the edge weights are symmetric, where the relationship between nodes is not directional ($a_{ij} = a_{ji}$).

In Eqn. (4), the *neighbor radius* (ε) is used to determine the number of neighbor nodes that connect to a particular node. Consider a node at the center of a sphere with radius ε; this node is connected to all nodes residing within the volume of this sphere. The edge weight of

each connection is given by the Euclidean distance term in Eqn. (4), whereas no connections are made to nodes falling outside the sphere (edge weight a_{ij} = 0).

The neighbor radius (ε) is a function of the average distance between adjacent nodes, d_{avg}, which is computed as $d_{avg} = \left(\frac{vol}{N}\right)^{1/3}$, where vol is the volume of the simulated part and substrate (simulated domain), and N is the number of nodes in the domain. Once the adjacency matrix (A) is formed, the diagonal degree matrix (D) entries are easily calculated as the row-wise sum of all adjacency matrix entries, given by

$$d_i = \sum_{j=1}^{N} a_{ij}$$
$$D = \begin{bmatrix} d_1 & \cdots & 0 \\ \vdots & \ddots & \vdots \\ 0 & \cdots & d_N \end{bmatrix} \quad (5)$$

From the adjacency matrix A and diagonal degree matrix D, the Laplacian matrix is defined as $L = (D - A)$. Next, eigenvalues and eigenvectors of the Laplacian matrix are obtained by solving the following equation using standard methods:

$$L\Phi = \Phi\lambda \quad (6)$$

$$\therefore L = \Phi\lambda\Phi^{-1} \quad (7)$$

Here Φ and λ are matrices for the eigenvectors and eigenvalues of the Laplacian matrix, respectively. A consequence of the symmetric edge weight formulation (un-directed graph) is a symmetric Laplacian matrix, which results in real (non-complex) eigenvalues. Substituting Eqn. (7) into Eqn. (1) gives an equation for temperature in terms of the material properties, the network graph and its connectedness, and the welding heat source, which gives the linear differential equation:

$$\frac{1}{\alpha}\frac{\partial T}{\partial t} = \Phi\lambda\Phi^{-1}T + \frac{1}{k}g \tag{8}$$

In the above, T is a discrete vector of temperatures at the nodes and g is the discrete vector of heat source strength at the nodes. Note that Eqn. (8) is discrete in space and a first order differential equation in time, whose solution has the form of exponential functions in time.

The nodal temperature distribution at an observation time, τ, is calculated as the sum of two terms: T_{in} caused by the initial temperature condition of the geometry, and T_g caused by volumetric internal heat generation (welding heat source) in the geometry [33]. That is, the temperature T is given as:

$$T = T_{in} + T_g \tag{9}$$

$$T_{in} = \Phi e^{-\lambda\tau}\Phi^{-1}T_0$$

$$T_g = \begin{cases} \Phi\lambda^{-1}\left(I - e^{-\lambda\tau}\right)\Phi^{-1}g & \text{during deposition} \\ \Phi\lambda^{-1}\left(e^{-\lambda(\tau-t)} - e^{-\lambda\tau}\right)\Phi^{-1}g & \text{during dwell} \end{cases}$$

Here, τ is the observation time at which the temperature is computed; t is the total time the block is heated; g is a local heating term; I is the identity matrix; and T_0 is the initial nodal temperature distribution. Details on the source term g are given in Section 3.3.

3.2 WAAM Process Simulation using the Spectral Graph Method

The thermal modeling of the WAAM process using the spectral graph method encompasses four steps, as illustrated in Figure 12.

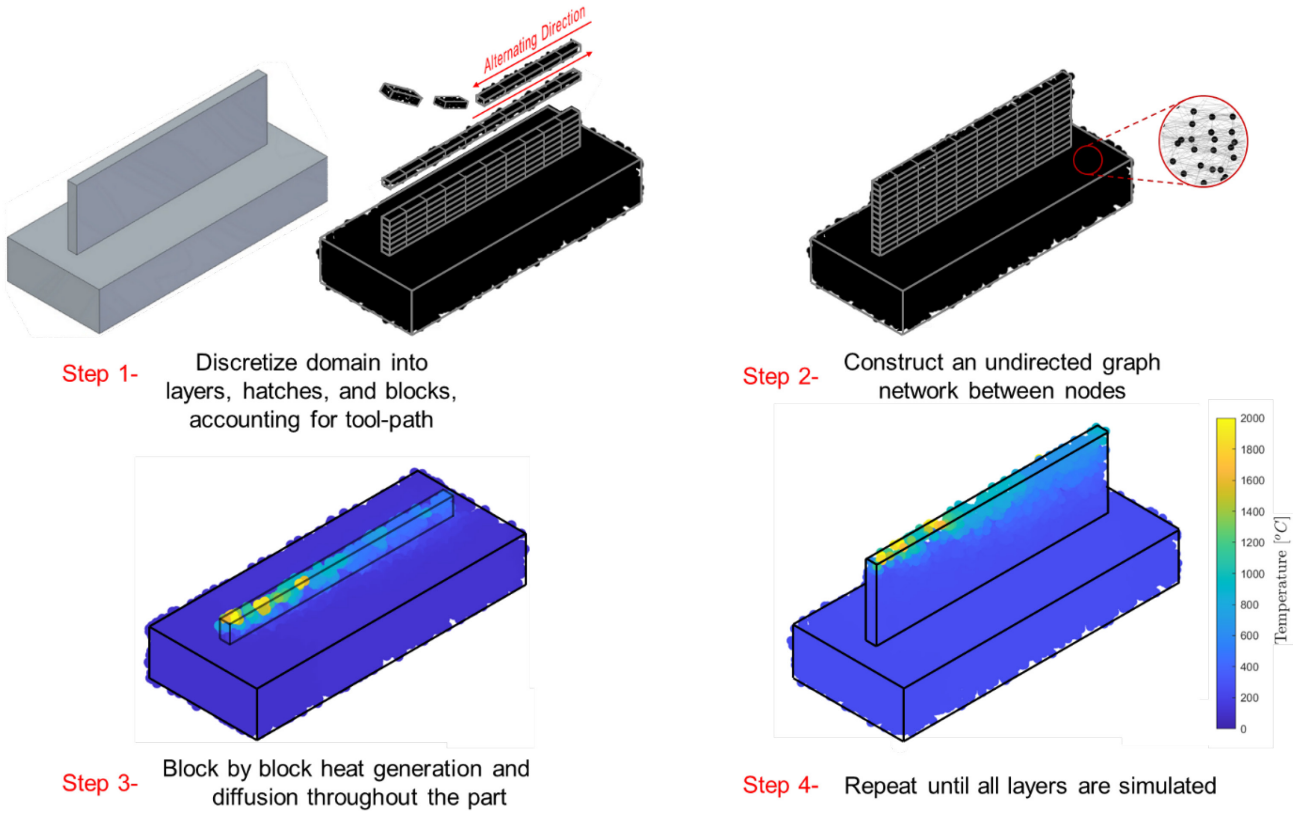

Figure 12: Steps taken to model the thermal history of the rectangle wall using the graph theory method.

Step 1: Discretization of the geometry with tool path consideration.

The first step of the spectral graph method concerns discretization of the geometry. Nodes are randomly generated to fill the part geometry, and substrate, such that an average nodal density is achieved throughout the simulation domain. The nodes represent discrete physical locations within the part boundaries where temperature responses will be computed. Each node is connected to nearby nodes through the mathematical relationship described in Eqn. (4) in Section 3.1.

Next, the part geometry is discretized into layers, hatches (weld tracks), and blocks as shown in Figure 13, to account for the locus of the welding torch (tool path) during the deposition process. The layers and hatches are discretized by the as-measured physical deposition layer height and hatch width (1.5 mm and 4.7 mm in this work, respectively). The spectral graph approach is also capable of directly using the input .STL file to determine the hatch width and layer height. A second alternative is to measure these from previous experimental parts manufactured under similar processing parameters.

Since this work is focused on part-scale thermal modeling, we used the as-produced part geometry measured to measure the layer height and the hatch spacing. Whilst multiple hatches may be deposited on a single layer, in this study, each thin-wall is deposited with a single hatch. Each hatch is further discretized into blocks of size 10 mm × 4.7 mm × 1.5 mm for the rectangle geometry; the width and height of each block are identical to the corresponding layer dimensions. Since each consecutive layer length reduces for the trapezoid geometry, the block lengths reduce evenly in size for each succeeding layer, distributing the reduction in layer length uniformly across all blocks on the layer.

The length of the block is an adjustable parameter in the model. An increase in block size reduces the computation time at the cost of prediction accuracy. This is because increasing the length of the block broadens the volumetric heating that represents the heat source.

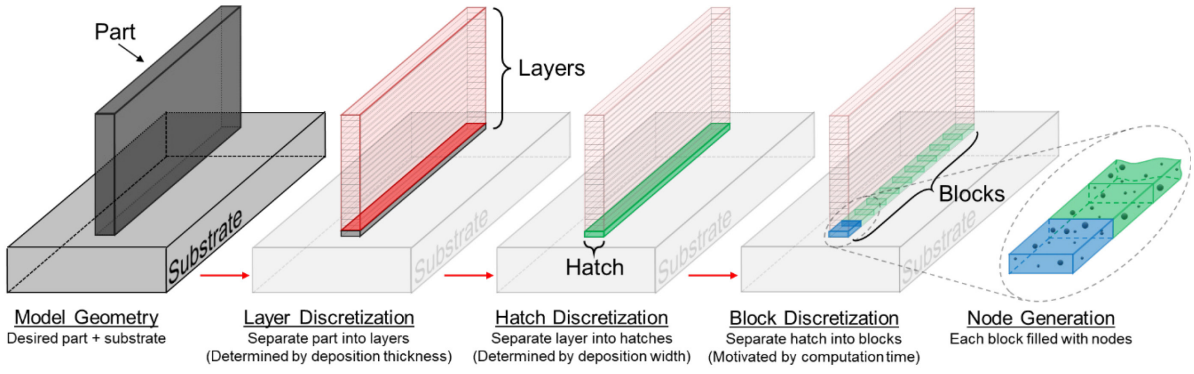

Figure 13: Geometry discretization for WAAM simulation of a single hatch rectangle wall.

Step 2: Establishing the connection between nodes (constructing a network graph)

After nodes have been placed in the body, a network graph is constructed over the nodes, and the corresponding Laplacian matrix is constructed by connecting nearby neighbors for each node and assigning a strength to each connection. The build deposition is simulated block-by-block, so a distinct Laplacian matrix is constructed as each block is added. Eqns. (4)-(7) describe the mathematical process for constructing the Laplacian matrix.

Step 3: Simulating deposition of material

Material deposition is simulated block-by-block, sequentially imitating the velocity and locus of the welding torch. After each block and its corresponding nodes are added, a heating cycle is initiated, and the thermal response is computed per Eqn. (9). A heating cycle consists of the following computational procedural sub-steps:

(a) material, represented by a block with nodes, is added to the model and the Laplacian matrix is constructed per Eqns. (4)-(7);

(b) nodes in the heat source region are heated per Eqns. (10)-(12) in Section 3.3; and

(c) the resulting temperature-in-time response for all nodes in the simulation domain is calculated per Eqn. (9).

Step 4: Repeat steps 2,3 for all blocks in the build

The temperature at the end of each heating cycle is the initial temperature for the next cycle, except for the nodes residing in the block that is to be deposited next, where the initial temperature is set to 1700 K, which is near to the liquidus temperature of mild steel [39]. The process is repeated until all blocks have been added for each hatch and all hatches have been added for each layer, followed by the appropriate dwell time after each hatch and/or layer, followed by the addition of all subsequent layers.

When the final block for a given layer is deposited, the corresponding computation cycle consists of a heating period followed by a dwell period which is defined by the interlayer dwell

time, t_d. During the dwell period, the heat source term does not contribute to the temperature-in-time calculation at observation time (τ) in Eqn. (9).

3.3 Heat Input – Energy Supplied by the Welding Torch

Simulation of thermal history in WAAM requires consideration of a localized, slow-moving heat source. To model heat input, Goldak et al. [40] developed a 3D double-ellipsoid heat density model for welding heat sources. The model is an extension of the heat source equation originally proposed by Rosenthal [41]. This double-ellipsoid model has proven to be useful for modeling various welding heat sources [42]. For example, Gery et al. [43] used the Goldak double-ellipsoid model to simulate heat input during butt welds in plate. Though the Goldak model is often used directly, minor application-specific modifications have been implemented in the literature [44]. Flint et al. [45] proposed and experimentally validated a double-ellipsoid based conical heat source model which was used to simulate a deep groove arc weld joint. Montevecchi et al. [46] proposed a model which segregates the heat input by assuming that half the energy supplied by the welding source is consumed by melting the feedstock wire, which is otherwise not considered.

Heat input during the WAAM process comes from a welding arc established between the feedstock (wire) and the previously deposited build and substrate. When simulating the deposition of a block, the total energy input per unit volume, q_{max} [$\mathrm{W \cdot mm^{-3}}$], is given by:

$$q_{max} = \frac{\text{heat input}}{\text{volume deposited}} = \frac{Q}{vol} = \frac{\eta V I}{\left(w_f \times \frac{\pi d^2}{4}\right) \times \frac{L_{block}}{v}} \tag{10}$$

where the heat input by the welding process, Q [W], is a function of the process efficiency, η, the weld voltage, V, and the welding current, I. Further, d is the diameter of the wire feedstock, w_f is the wire feed rate, L_{block} is the length of the simulation block, and v is the travel speed of the welding torch. Thus, the total energy input at the meltpool is estimated as a

function of the process parameters reported in Table 2. The denominator in Eqn. (10) is the volumetric flow rate of the feedstock (wire) multiplied by the time required to deposit one block. The time to deposit one block is the block length, L_{block}, divided by the travel speed of the welding torch, v.

Following the work of Goldak et al., (1984), the heat density q has an ellipsoidal distribution given by:

$$q(x_i, y_i, z_i) = \frac{6\sqrt{3}}{\pi\sqrt{\pi}} Q \times \frac{1}{r_x} e^{\frac{-3(x_i - x_0)^2}{r_x^2}} \times \frac{1}{r_y} e^{\frac{-3(y_i - y_0)^2}{r_y^2}} \times \frac{1}{r_z} e^{\frac{-3(z_i - z_0)^2}{r_z}} \quad (11)$$

where the maximum heat density, $q(0)$, occurs at the center of the ellipsoid, (x_0, y_0, z_0), and the parameters r_x, r_y, r_z, are the cartesian ellipsoidal radii which provide the size of the power density distribution. In the current work, an added step is required to construct the volumetric internal heating vector, g, which specifies the energy input at discrete nodes in a heated region. First, nodes residing within the heated region, which is defined by the surface of the ellipsoid, shown in Figure 14, are assigned a volumetric power density using the distribution function given in Eqn. (11), where x_i, y_i, z_i, are the cartesian coordinates for node i. Next, a scaling factor is found by taking the ratio of the maximum possible power density, q_{max}, and the sum of the power density from the heated nodes. The scaled volumetric internal heating value for each heated node, g_i, is given by:

$$g_i = \left(\frac{q_{max}}{\sum q_i}\right) \times q_i \quad (12)$$

where the sum is over the heated nodes.

The size of the ellipsoid is independent of the size of the simulation block; however, the ellipsoid is centered on the simulation block for each heating cycle. This approach provides heat input at the center of the deposited block, simulating the slow-moving heat source used

during WAAM processing. The heat source modeling parameters used for the thermal simulation are given in Table 3.

Thus, the spectral graph theory model inherently accounts for meltpool temperature and distribution via the Goldak approximation. Moreover, in cold metal transfer welding, which is used in this work, deleterious effects such as superheating of the meltpool are atypical and were not observed during deposition.

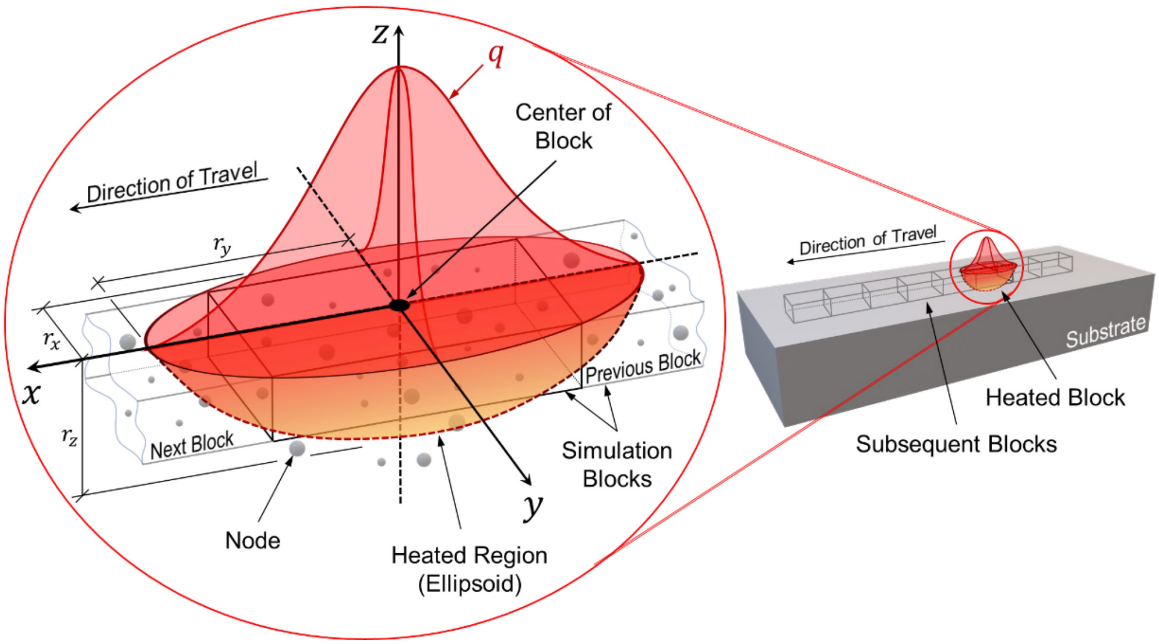

Figure 14: Ellipsoidal power density distribution centered on a simulation block. Nodes within and surrounding the block are heated, simulating a localized heat source provided by the welding arc.

Table 3: Simulation parameters for rectangle and trapezoid thin-wall cases.

Variable		Value
Material properties	Density, ρ [kg·m^{-3}]	7700
	Specific heat, C_p [J·kg^{-1}·K^{-1}]	801.9
	Thermal conductivity, k [W·m^{-1}·K^{-1}]	34.2
Internal heat generation	Torch speed, v [mm·s^{-1}]	11.67
	Weld voltage, V	14.8
	Weld current, I [Amperes]	110
	Weld efficiency, η [%]	90
	Heated region radii, r_x, r_y, r_z [mm]	5, 2.35, 1.5
	Initial temperature of nodes in deposition block [K]	1700
Working variables	Ambient temperature, T_∞ [K]	300
	Dimensions of simulation block [mm]	$10 \times 4.7 \times 1.5$

3.4 Boundary Heat Loss

As heat diffusion occurs within the part, heat loss to the surrounding is experienced due to radiation and convection, as previously shown in Figure 3, Section 1.2.2. To simulate boundary heat loss, four regions were chosen, each of which represent different levels of effective heat loss from the part. The use of four regions was chosen to reflect the heat loss mechanisms present while restricting the number of parameters to be determined during calibration of the model.

For the current work, the top-most three layers are subjected to radiation heat loss as well as forced convection provided by the continuous flow of shielding gas from the welding torch. Referring to Figure 15, heat loss coefficient h_1 describes the top-most three layer region. The remaining layers in the wall are described by heat loss coefficient h_2, which is smaller in

magnitude than h_1, for the reduced effect of radiation as well as a reduced forced convection due to the lower velocity of shielding gas.

The top surface of the substrate is assigned heat loss coefficient h_3, which is smaller yet, accounting for natural convection along with a small contribution of forced convection from the flow of shielding gas. Lastly, the bottom and sides of the substrate are assigned heat loss coefficient h_4, which represents natural convection only. The boundary heat loss coefficient regions, which encompass the effects of radiation and free and forced convection, are shown in Figure 15. Values for heat transfer coefficients are found from calibration of the model, which is discussed in Section 4.1.

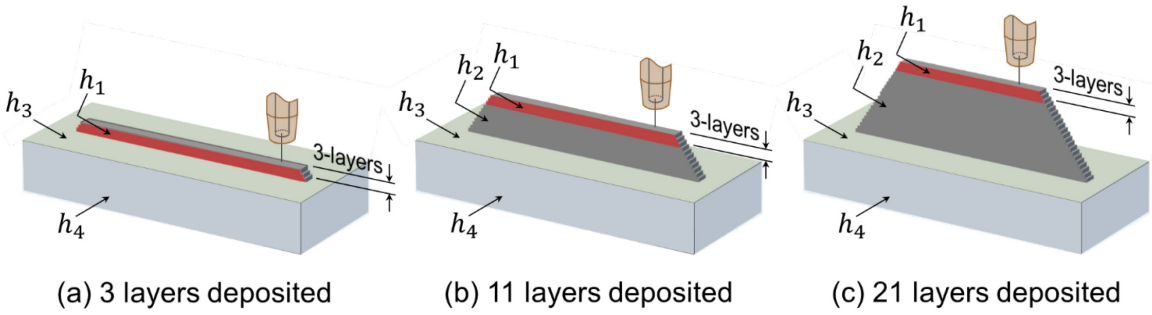

Figure 15: Heat loss regions used for simulation, shown at various stages of the build with: (a) 3 layers deposited, (b) 11 layers deposited, (c) 21 layers deposited. The top-most 3 layers at any time in the simulation are assigned heat loss coefficient h_1. All remaining previously deposited layers are assigned heat loss coefficient h_2. The top surface and side and bottom surfaces of the substrate are assigned heat loss coefficients h_3 and h_4, respectively.

To include the effects of these heat loss coefficients in the graph theory method, the edge weights in the Laplacian matrix corresponding to boundary nodes must be adjusted. If a node resides near the boundary, a boundary heat loss term, E_j, is added to the diagonal entry of the Laplacian matrix. The boundary heat loss term is found through an energy balance for a node at the boundary, and is given as:

$$E_j = \frac{A_j}{V_j}\left(\frac{Bi}{1 + Bi \cdot \frac{e_j}{\ell}}\right) \tag{13}$$

where A_j is the surface area for heat transfer, calculated as the total surface area of the part and substrate divided by the total number of boundary nodes; V_j is the nodal volume, calculated as the total volume of the part and substrate divided by the total number of nodes in the simulation; $Bi = h_i \ell / k$ is the Biot number, $i = 1,2,3,4$; here ℓ is the characteristic length; and, e_j/ℓ is the (normalized) orthogonal distance from the node j to the boundary. The value of ℓ in Eqn. (13) is a direct consequence of the sum of two thermal resistors appearing in the denominator of the energy balance for a boundary node. A full discussion of boundary heat loss for the spectral graph method, as well as the derivation of Eqn. (13), is given by Cole et al. [33].

4. Results

Before using the developed spectral graph method, model calibration through parameter estimation was conducted. Experimental data from the *Trap43* build, whose collected thermocouple data is shown in Figure 10, was used for calibration. The spectral graph method is then verified by comparison with an FE analysis for the *Rect43* experimental case.

The FE analysis was carried out using a combination of Abaqus for meshing and Simufact Welding v7.1 for the thermal simulation. After the model calibration was complete, all remaining experimental cases were simulated using the spectral graph method and the predictions are compared with experimental data without further calibration. The model prediction error is quantified in terms of two metrics, namely, the symmetric mean absolute percentage error (SMAPE), and the root mean squared error (RMSE).

4.1 Model Calibration

Model parameters requiring calibration are the gain factor f and the effective heat loss coefficients, $h_i, i = 1,2,3,4$. The gain factor is calibrated for a node density, irrespective of the simulation geometry. The gain factor f, used in Eqn. (4), is tuned by simulating a benchmark heat transfer problem for a simple cuboid-shaped geometry, discussed in detail by Cole et al. [33]. The benchmark heat transfer problem is solved using an exact Green's function-based solution, which is then compared with the spectral graph solution for different values of the gain factor. An iterative Gauss-Newton algorithm is used to minimize the sum of squared error between the exact and spectral graph solutions.

The effective heat loss coefficients, h_i, are calibrated through a grid search using the experimental data from the *Trap43* experiment (a) with respect to data from thermocouple TC3. The *Trap43* case was chosen because it is relatively more complex shape than the rectangle geometry. As mentioned in Section 3.1, the effective heat loss coefficients account for all heat loss mechanisms, including heat loss due to radiation and both free and forced convection. Once calibrated, these parameters were applied to the simulation of the five remaining cases with two experiments for each case (*Rect43, Rect86, Trap86, Trap5×, Trap10×), and Trap43 experiment (b).* Further, for each case data from 4 thermocouple positions were acquired. In other words, a total of 48 independent temperature trends are available (6 shapes × 2 replications × 4 thermocouple locations). Out of these 48 available temperature trends only one trend, i.e., *Trap43* experiment (a) from thermocouple TC3 was used for calibration. The calibrated values for a node density of 0.12 nodes·mm^{-3} are given in Table 4. Lastly, our previous works in laser powder bed fusion additive manufacturing reported in Yavari et al. [30, 31] and Riensche et al. [38] show that once calibrated these heat transfer parameters can be used for other geometries as long as the material and gas flow conditions are similar.

In calibrating both the gain factor and the heat loss coefficients, the weld efficiency, discussed in Section 3.3, is held constant. Though parameter estimation is effective for determining quantities that are particularly challenging to measure experimentally, such as heat loss coefficients, it can be stated that the calibrated values shown are not necessarily unique in their ability to support predictions of the experimentally observed temperature trends. That is, the weld efficiency and choice of representative heat loss regions are contributing factors in the calibration of heat loss parameters.

Table 4: Calibrated graph theory model parameters used for simulating all rectangle and trapezoid thin-wall cases. Node density, Gain factor f, and effective heat loss coefficients $h_i, i = 1,2,3,4$.

Node Density [nodes·mm^{-3}]	0.12	
Gain Factor f [unitless]	0.77	
Heat Loss Region and Coefficient [W·m^{-2}·K^{-1}]	h_1	200
	h_2	100
	h_3	40
	h_4	2

The thermocouples used were K-type, installed in a metal sheath, with an air gap between the thermocouple bead and the sheath. These are ungrounded thermocouples, which are known to have a lengthy time-constant, effectively dampening rapid temperature variations in the recorded thermocouple response [47]. Hence, an 11.25 s response time was used for filtering the simulated thermal history, which corresponds to five times the time-constant for a 5 mm diameter ungrounded K-type thermocouple. See Appendix C for details on the filtering procedure.

4.2 Model Verification – Comparison with FE-based Simufact Welding Software

The following results demonstrate that the trend and magnitude of the thermal history predicted by the spectral graph theory approach matches closely with those obtained by a commercial FE-based package (Simufact Welding v7.1). The predicted thermal history trends are accurate at not only for the part-level, but also match at layer-level. Further, the spectral graph theory approach converges twice as fast as the commercial FE package.

4.2.1 Verification of Part-level Thermal History

Verification is carried out by comparison between the predicted part-level thermal histories obtained from the spectral graph method and from Simufact Welding v7.1, a commercially available FE software, for the *Rect43* experimental case. The calibrated heat loss coefficients used for the spectral graph method, described in Section 4.1, Table 4, are used as inputs to the FE software as well as the process parameters, shown in Table 3.

The meshing of the substrate and each weld bead was done in Abaqus, another commercially available software. The number of elements were selected such that the level of prediction error using Simufact was similar to the spectral graph theory prediction. The simulation mesh is assembled in Simufact manually, with each weld bead requiring user-assigned boundary conditions and heat source parameters. Each weld bead (layer) is comprised of 1,536 elements and 2,709 nodes. The substrate is comprised of 115,200 elements and 124,509 nodes. All elements were of type C3D8R, which are general purpose linear brick elements and feature reduced integration (one integration point). The total mesh, inclusive of the substrate and all 21 layers, contains 147,456 elements and 181,398 nodes.

The FE-based Simufact model converged in ~7.5 hours compared to under 4 hours for the spectral graph theory model. To quantify the agreement between the experimental thermocouple data, Simufact, and the spectral graph predictions, the symmetric mean absolute percent error (SMAPE) and root mean squared error (RMSE, °C) metrics are used. The reference case for calculating the SMAPE and RMSE values is the first experimental replicate (Experiment (a)) for *Rect43* and *Rect86*. Consistent with the spectral graph method, the Simufact FE analysis predicts thermal history at the thermocouple location without consideration of the thermocouple time delay present. Hence, the 11.25 s response time used for filtering the spectral graph results was also applied to the Simufact simulation. This allows for a comparison between the experimentally obtained thermocouple data and the predictions

from both the spectral graph method and the Simufact Welding FE analysis. The method used for filtering the thermal trends is detailed in Appendix C.

Figure 16(a) and (b) shows the thermal histories obtained from the experiment as well as from the spectral graph and Simufact simulations for thermocouple location 3 (TC3) for the *Rect43* and *Rect86* cases, respectively. The Simufact predicted thermal trends agree well with both the experimental data and the spectral graph predictions for both cases. In the *Rect86* case, Figure 16(b), the Simufact FE analysis predicts a buildup of heat until the midpoint of the build, after which the heat loss causes the thermocouple response to have a downward trend.

In contrast, the spectral graph method prediction agrees well through the entirety of the *Rect86* build. Observe that the difference in shape of the layer-wise thermal response between the cases is well captured by both the Simufact and spectral graph simulations, where the temperature elevations are more pronounced in the *Rect86* case as compared to the *Rect43* case. To quantify the agreement between the experimentally collected data and the Simufact prediction at the TC3 location for the *Rect43* case, the SMAPE and RMSE values are calculated to be 1.8% and 7.6 °C, respectively. In comparison, the SMAPE and RMSE values describing the agreement between the *Rect43* experimental data and the spectral graph prediction are 3.3% and 13.2°C, respectively. For the agreement between the *Rect86* experimental data and the Simufact prediction, the SMAPE and RMSE values for the TC3 location are calculated to be 3.5% and 13.8 °C, respectively. In comparison, the SMAPE and RMSE values describing the agreement between the *Rect86* experimental data and the spectral graph prediction are 1.7% and 5.6 °C, respectively.

Figure 17 shows the 3D temperature distribution as predicted by the Simufact FE analysis and the spectral graph method for the *Rect43* and *Rect86* cases, immediately after deposition is completed for the 5^{th}, 10^{th}, 15^{th}, and 20^{th} layers. Comparing the temperature distributions

qualitatively, local variation is seen in the spectral graph results where the thermal field is less smooth than that produced by the Simufact FE analysis.

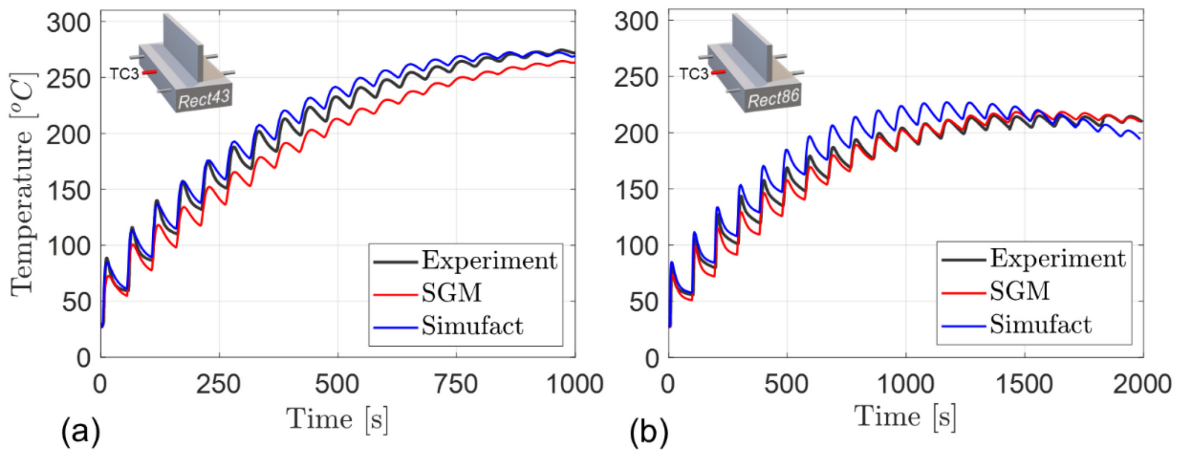

Figure 16: Verification of the spectral graph method (SGM) by comparison with predictions obtained from a commercial finite element analysis software (Simufact Welding v7.1) at thermocouple location 3 (TC3) for (a) the *Rect43* rectangular thin-wall case with a constant 43 second interlayer dwell time ($t_d = 43$ s), and (b) the *Rect86* rectangular thin-wall case with a constant 86 second interlayer dwell time ($t_d = 86$ s).

The foregoing result demonstrates that the part-scale thermal distributions agree well between the Simufact and spectral graph method predictions. In the spectral graph method, the temperatures are calculated at discrete nodes which are randomly placed throughout the part. The stochasticity of the node locations contributes to the local temperature variation since the internodal heat conduction is dictated by the strength of the connection between nearby nodes, which is determined by the proximity of the nodes.

As demonstrated in Figure 16 and detailed in Table 5, the part scale temperature distribution predicted by Simufact Welding and by the spectral graph method are in agreement, and the thermal gradients are captured from the deposition layer through to the substrate. The calculated SMAPE and RMSE values for all of the thermocouple locations for both the *Rect43* and *Rect86* cases are tabulated in Table 7.

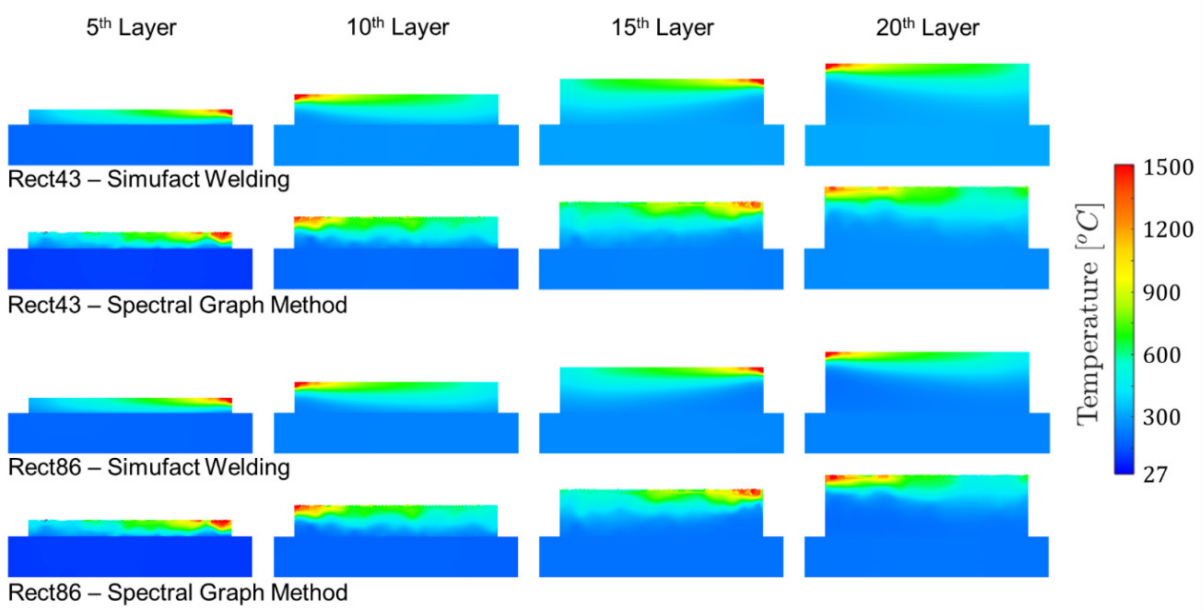

Figure 17: Simulated 3D temperature distributions obtained from an FE analysis (Simufact Welding v7.1) and from the spectral graph method showing the temperatures predicted at the instant the torch completes deposition of the 5th, 10th, 15th, and 20th layers for case *Rect43* with 43 s interlayer dwell time.

Table 5: Symmetric mean absolute percentage error (SMAPE) and root mean square error (RMSE), calculated by comparison between Simufact Welding simulation results and experimental data as well as between the spectral graph method simulation results and experimental data for all thermocouple locations in experiments *Rect43* and *Rect86.*

Case		Rect43		Rect86	
Modelling Method		Simufact Welding	Spectral Graph	Simufact Welding	Spectral Graph
SMAPE [%]	TC1	5.58	2.11	8.28	5.31
	TC2	4.70	2.51	5.67	3.69
	TC3	1.82	3.27	3.51	1.67
	TC4	2.66	2.84	3.81	2.44
RMSE [°C]	TC1	22.13	7.82	29.45	19.08
	TC2	18.43	10.84	21.13	14.28
	TC3	3.30	13.19	13.75	5.64
	TC4	10.52	10.67	14.81	8.67

4.2.2 Verification of Layer-level Thermal History

Continuing with the analysis, we compared the spectral graph and Simufact FE thermal history predictions for certain layers. Further, this analysis addresses the experimental drawback in not having thermocouples welded to the part. Specifically, tracked in Figure 18 and Figure 19, respectively, are the thermal histories of layer 7 and layer 13 for select rectangle and trapezoid cases. The solid red and dashed blue lines are thermal predictions obtained from

the spectral graph and Simufact software, respectively. The thermal history is reported at the midpoint along the layer. The RMSE and SMAPE of the spectral graph predictions relative to the Simufact FE predictions are reported in table 6. The SMAPE was within 8% for all tested cases (~2% best case scenario).

We note that these temperatures predicted are substantially larger than the part-level temperatures recorded by the thermocouples embedded in the substrate. For example, reported in Figure 18(a) is the thermal history for layer 7 of *Rect43*. The first peak therein is the temperature at the bottom of layer 7 when the welding torch is depositing layer 9 overhead. The temperature corresponding to the first peak exceeds 750 °C, which is larger than $0.5 \times T_m$ (melting point of the material). Subsequent peaks correspond to layers 10, 11, 12, and so on, when the torch is directly overhead the sampling region at the midpoint of layer 7. As expected, the magnitude of temperature and oscillations at layer 7 decay progressively with deposition of further layers. The spectral graph- and Simufact-derived temporal thermal trends match in terms of both the shape and magnitude.

Table 6: Symmetric mean absolute percentage error (SMAPE) and root mean square error (RMSE), calculated by comparing thermal predictions obtained from the spectral graph method and Simufact Welding. The thermal predictions are compared for layers 7 and 13 of Rect43, Rect86, Trap43, and Trap86 cases.

Rectangle Cases	SMAPE [%]	RMSE [°C]	Trapezoid Cases	SMAPE [%]	RMSE [°C]
Rect43 - Layer 7	2.90	38.24	Trap43 - Layer 7	2.12	24.16
Rect43 - Layer 13	6.33	82.37	Trap43 - Layer 13	3.59	26.20
Rect86 - Layer 7	3.58	36.04	Trap86 - Layer 7	3.46	25.12
Rect86 - Layer 13	7.65	76.93	Trap86 - Layer 13	4.32	22.54

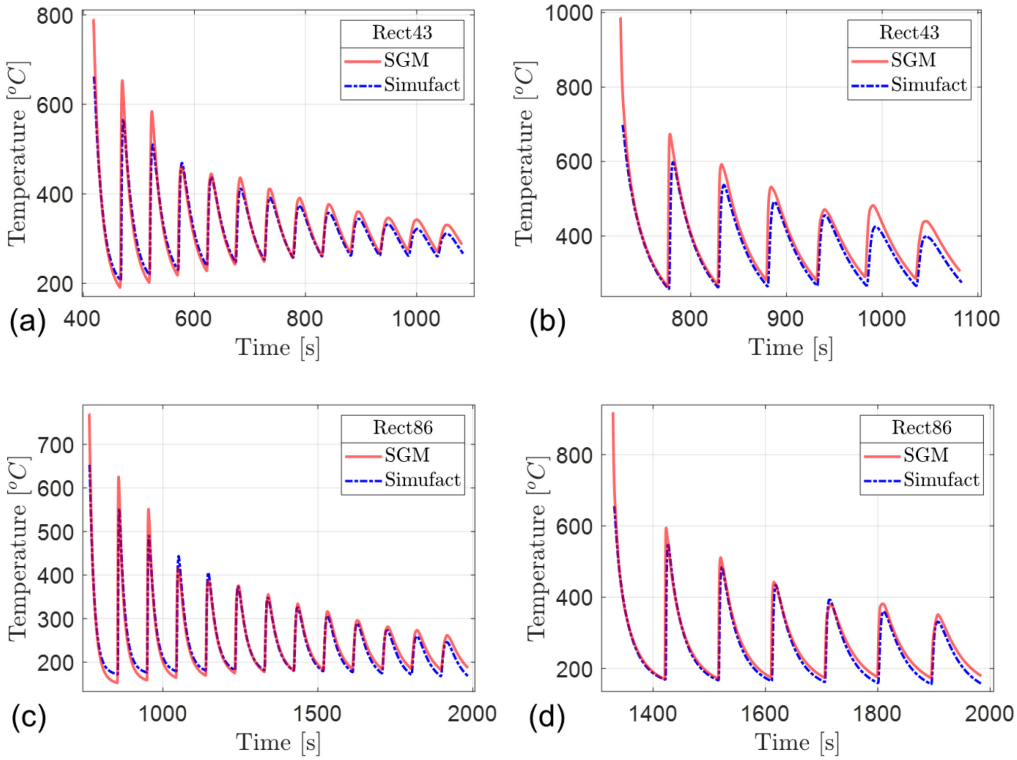

Figure 18: Simulated thermal history at selected layers obtained from an FE analysis (Simufact Welding v7.1, dashed blue line) and from the spectral graph method (solid red line) for the rectangular cases. (a) Rect43 - Layer 7, (b) Rect43 - Layer 13, (c) Rect86 - Layer 7, and (d) Rect86 - Layer 13. Note the close match in the trend and magnitude of the thermal predictions.

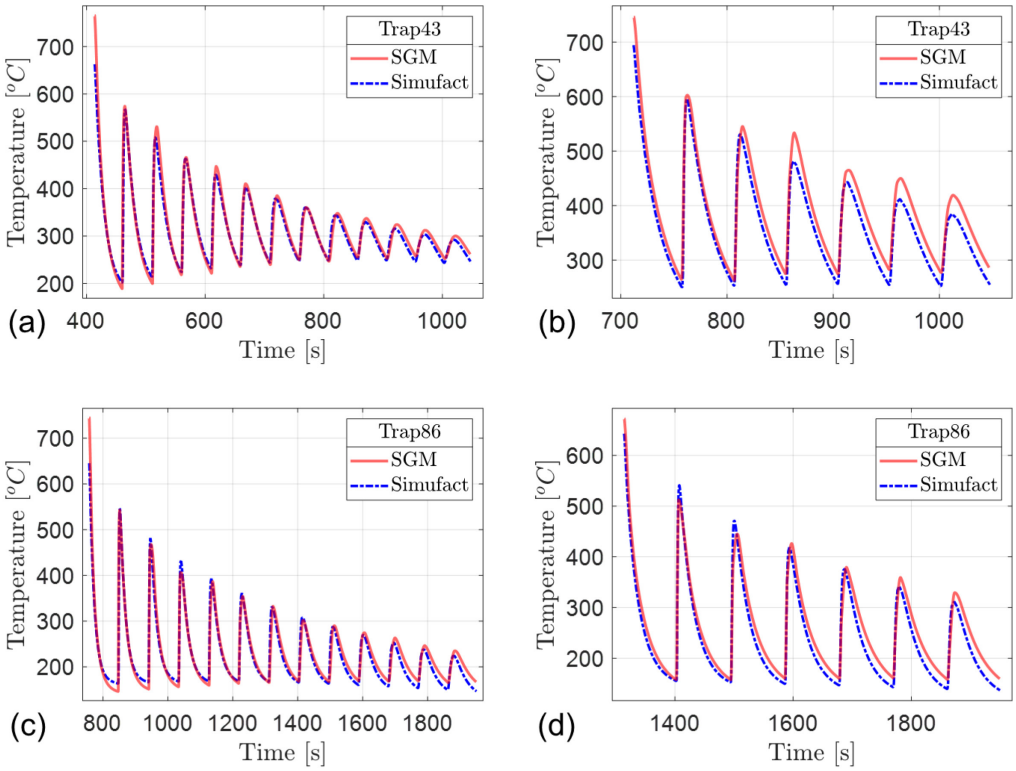

Figure 19: Simulated thermal history at selected layers obtained from an FE analysis (Simufact Welding v7.1, dashed blue line) and from the spectral graph method (solid red line) for the trapezoid cases. (a) Trap43 – Layer 7, (b) Trap43 - Layer 13, (c) Trap86 - Layer 7, and (d) Trap86 - Layer 13. Note the close match in the trend and magnitude of the thermal predictions.

4.3 Model Validation

To validate the spectral graph method for thermal history modeling in WAAM, the spectral graph simulated and experimentally observed temperature trends at the thermocouple locations are compared. For brevity, only the comparison corresponding to thermocouple location 3 (TC3) is discussed in this section. A similar discussion for thermocouple locations 1, 2, and 4 is given in Appendix B. Simulated 3D temperature distributions after the completion of deposition at various layers is also provided to qualitatively demonstrate the part-scale thermal gradients captured by the model.

For all cases, a node density of 0.12 nodes·mm^{-3} was used, amounting to 15,408 and 15,129 nodes for the rectangle and trapezoid geometries, respectively. A desktop AMD Ryzen 3970X CPU, clocked at 3.7 GHz, with 128 GB RAM was used for all numerical simulations. Since the available experimental data was collected using thermocouples located within the substrate, temperatures near to the meltpool were not captured and analyzed.

In the literature, authors often utilize thermal history data collected from the substrate to validate thermal models, with the motivation that heat source models affect both the near and far-field thermal responses, yielding accurate models validated using far-field thermal data [48]. For example, Hackenhaar et al. [49] studied the effect of air jet impingement during the processing of WAAM parts. They utilized three thermocouples at the substrate to validate their FE model by comparing their predicted thermal history with that of the experiment. Zhou et al. [50] studied the effect scan strategies had on temperature history in P-DED parts. They used a single thermocouple on the top and bottom surfaces of their substrate to collect experimental thermal data, which was then compared with their predicted thermal history at the same locations to validate their FE model. Chen et al. [48] studied part scale residual stress in the LPBF process. They used three thermocouples mounted to the bottom of the substrate to collect thermal history data which was then used to validate their FE model by comparison with their

predicted thermal history at the same locations. Yang et al. [51] studied the thermomechanical behavior of Ti-6Al-4V parts produced using the laser engineered net shaping (LENS) DED process. Their study used two thermocouples, one on the top surface and the other on the bottom surface of the substrate to collect thermal history data. The experimentally observed thermal history was then compared with their FE predicted thermal history for validation.

We note that the thermal data collected in this study is used for validation of the spectral graph method. The temperature trends predicted by the spectral graph theory approach is compared with the experimental data at the thermocouple locations. The SMAPE and RMSE metrics are used to quantify the agreement between the experimental measurements and model predictions. The reference case for calculating the SMAPE and RMSE values is the first experimental replicate (experiment (a)) for each of the six cases.

4.3.1 Rectangle Thin-wall Experiments

In Figure 20(a) and (b), the spectral graph simulated thermal trends are juxtaposed with the experimentally observed temperature trends at thermocouple location 3 (TC3) for cases *Rect43* and *Rect86*, respectively. Note, the thermal data for both experimental replicates are plotted. For the *Rect43* case, the overall thermal trend agrees well with the experimental data, with only a slight difference in magnitude for each layer. The SMAPE and RMSE for the *Rect43* case are calculated to be 3.3% and 13.2°C, respectively.

For the *Rect86* case, the agreement between the prediction and the experimental data is very good, with the spectral graph prediction having similar layer-wise magnitudes in the beginning half of the build and the overall trend falling within that of the experimental replicates for the latter half of the build. The SMAPE and RMSE for the *Rect86* case are calculated to be 1.7% and 5.6°C, respectively. The simulation time is less than 4.1 hours for each case.

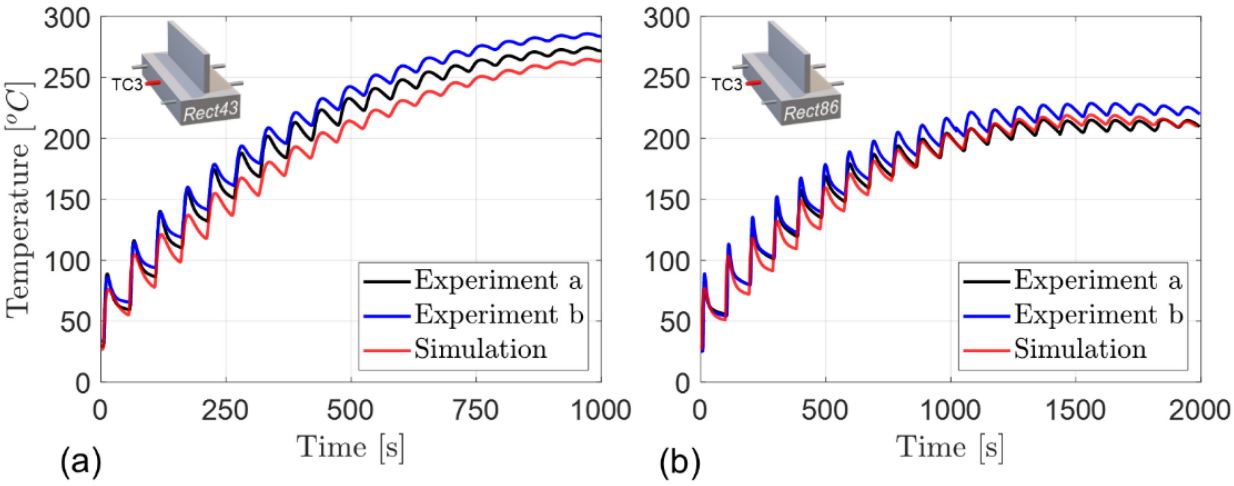

Figure 20: Thermal history comparison between experimental data and the graph theory thermal simulation at thermocouple location 3 (TC3) for: (a) *Rect43* rectangular thin-wall with a constant 43 second interlayer dwell time ($t_d = 43$ s), and (b) *Rect86* rectangular thin-wall with a constant 86 second interlayer dwell time ($t_d = 86$ s). The simulation time was less than 4.1 hours for each case.

A qualitative view of the spectral graph simulated 3D temperature distribution 40 s after the completion of deposition on the 5th, 10th, 15th, and 20th layers is shown in Figure 21 for both *Rect43* and *Rect86* cases. At the time instant shown, the interlayer dwell time is nearly complete for the *Rect43* case. In contrast, there are 46 s of interlayer dwell time remaining for the *Rect86* case, allowing for significant cooling before the next layer is deposited.

Considering that, at the time instant shown, the same amount of time has elapsed since the conclusion of deposition for the respective layer, the difference between the temperature distributions is the direct effect of the difference in interlayer dwell times. The difference is increasingly noticeable as the progression of the build furthers, where the 5th layer thermal distributions differ minimally compared to the 20th layer thermal distributions.

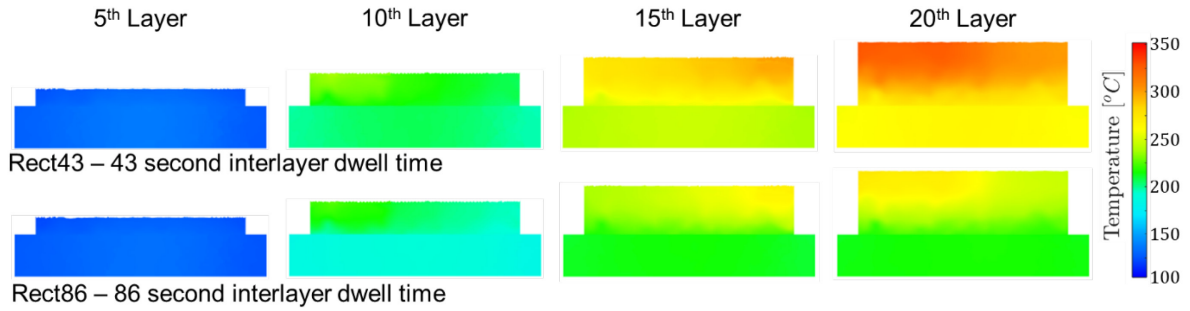

Figure 21: Simulated temperature distribution 40 s after deposition of the 5th, 10th, 15th, and 20th layers for cases *Rect43* and *Rect86* with 43 s and 86 s interlayer dwell times, respectively. Note the heat build-up in case *Rect43* compared to case *Rect86*.

4.3.2 Trapezoid Thin-wall Experiments

In Figure 22(a) and (b), the spectral graph simulated thermal trends are plotted with the experimentally observed temperature trends at thermocouple location 3 (TC3) for cases *Trap43* and *Trap86*, respectively. We note that model heat-loss parameters were calibrated from the *Trap43* data set from thermocouple TC3 of experiment (a). In Figure 22(a) these parameters were directly used for validation with *Trap43* data set from experiment (b). The *Trap43* data from experiment (a) is shown for completeness. For the *Trap43* experiment (b), the observed data agrees well with the trends predicted by the spectral graph method, with the calculated SMAPE and RMSE being 2.5% and 10.3°C, respectively.

For the *Trap86* case, the layer-wise heating, as seen by the magnitude of the peaks, matches well with the experimental data for the beginning of the build with a reduction in magnitude toward the late part of the build. Considering the model, the impact of the increased interlayer dwell time is apparent, where the simulated temperature at the thermocouple locations undershoots the experimental observations. Regardless, the overall simulated thermal trend for the *Trap86* case agrees well with the experimental data, with the SMAPE and RMSE values calculated as 3.4% and 10.9°C, respectively. The simulation time is less than 3.5 hours for both the *Trap43* and *Trap86* cases.

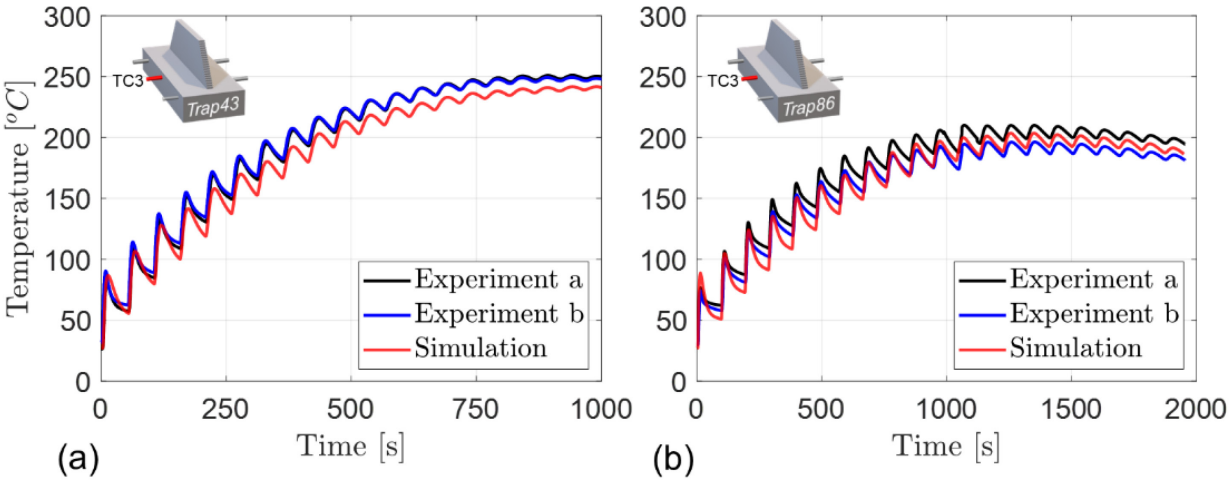

Figure 22: Thermal history comparison between experimental data and the graph theory thermal simulation at thermocouple location 3 (TC3) for: (a) *Trap43b* trapezoidal thin-wall with a constant 43 second interlayer dwell time ($t_d = 43$ s), and (b) *Trap86a and b* trapezoidal thin-wall with a constant 86 second interlayer dwell time ($t_d = 86$ s). Note that the model is calibrated with Trap43 data from Experiment (a). The simulation time was less than 3.5 hours for each case.

Figure 23 provides a qualitative view of the spectral graph simulated 3D temperature distribution after 40 s of interlayer dwell time has elapsed after deposition of the 5th, 10th, 15th, and 20th layers. The increased interlayer dwell time in case *Trap86* mitigates heat build-up when compared to case *Trap43,* as evidenced by the elevated temperatures in both the substrate and wall of the *Trap43* case. The heat build-up in the *Trap43* case is focused near the middle of the wall as opposed to one of the edges, as seen in the rectangle simulations. Since each layer is progressively shortened in the trapezoid cases, the thermal mass at the beginning and end of the previous layers, which does not experience subsequent deposition, serves to dampen the temperature rise at the far left and right, leaving the heat to accumulate near the midpoint of the thin-wall.

In Figure 24(a) and (b), the thermal trends predicted by the spectral graph method are plotted along with the experimental observations for thermocouple location 3 (TC3) for cases *Trap5*× and *Trap10*×, respectively. The data collected during both experimental replicates for each case are included in the plots. For the *Trap5*× case, the simulated thermal history agrees well with the experimental data, with the end of cycle temperatures (peaks) matching within a few °C throughout the entirety of the build. The end of build temperature is also predicted well,

as seen by the closeness in the final temperatures plotted. For the *Trap5×* case, the SMAPE and RMSE are calculated to be 1.5% and 6.2°C, respectively. For the *Trap10×* case, the temperature agreement matches well with SMAPE and RMSE calculated to be 3.2% and 12.1°C. Recall, the SMAPE and RMSE metrics are calculated and reported based on the first experimental replicate (experiment(a)).

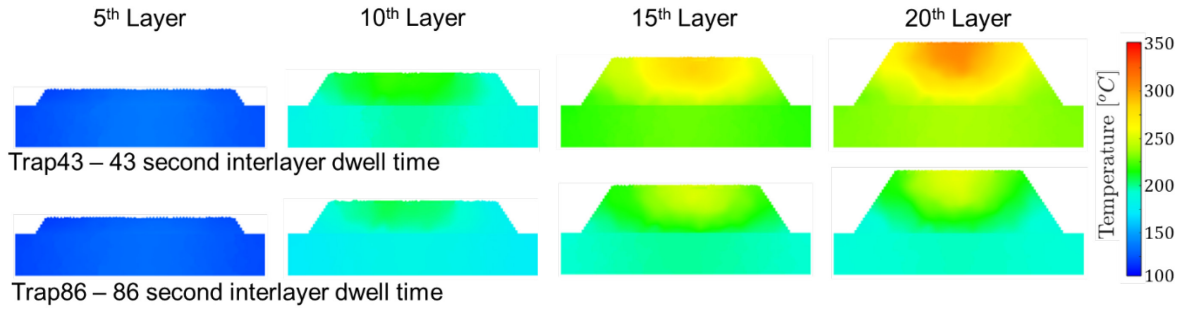

Figure 23: Simulated temperature distribution 40 s after deposition of the 5th, 10th, 15th, and 20th layers for cases *Trap43* and *Trap86* with 43 s and 86 s interlayer dwell times, respectively. Note the heat build-up in case *Trap43* compared to case *Trap86*.

There is close agreement between measurement and model predictions with the second experimental replicate (experiment (b)) for the *Trap10×* case. Of note is the slight disagreement between the peak locations on the plots in Figure 24. This difference is attributed to the experimental conditions where managing the dynamic interlayer dwell time and the wall-clock time presents difficulty during the experiment. The takeaway here is the overall agreement between the simulated thermal trends and the experimental data for both trapezoid cases having dynamic interlayer dwell times, where the overall temperature rise in the substrate caused by the WAAM process is predicted by the model. For both *Trap5×* and *Trap10×*, the simulation time is less than 3.5 hours for each case.

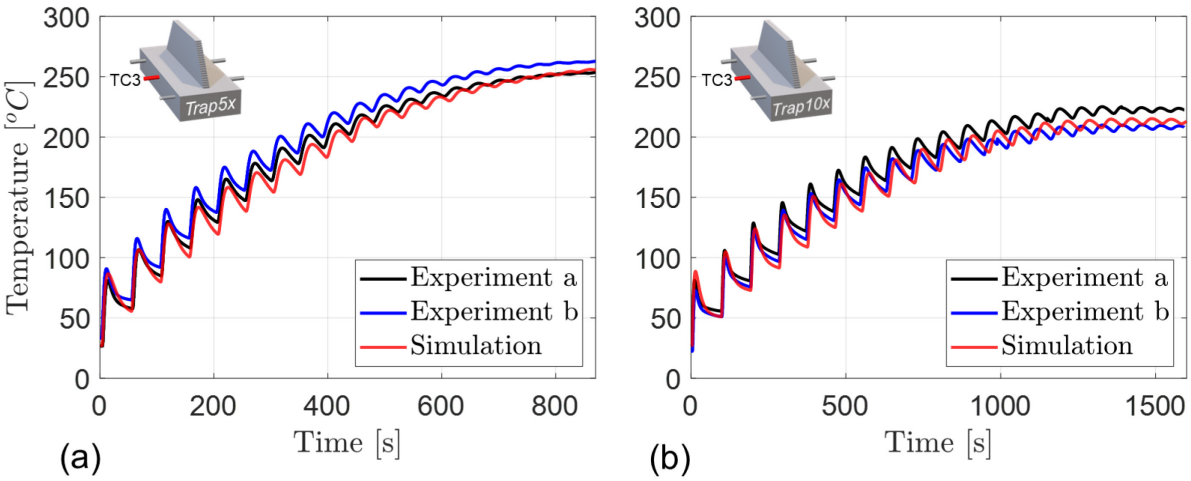

Figure 24: Thermal history comparison between experimental data and the spectral graph simulation at thermocouple location 3 (TC3) for: (a) *Trap5*× trapezoidal thin-wall with a non-constant interlayer dwell time equal to 5× the time taken to deposit the previous layer ($t_d = 5 \times t_{i-1}$) and, (b) *Trap10*× trapezoidal thin-wall with a non-constant interlayer dwell time equal to 10× the time taken to deposit the previous layer ($t_d = 10 \times t_{i-1}$).

Figure 25 provides a qualitative view of the spectral graph simulated 3D temperature distribution during the interlayer dwell time after the 5th, 10th, 15th, and 20th layers have been deposited for both *Trap5*× and *Trap10*× cases. The time instant shown, for both cases, corresponds to the end of the interlayer dwell time for the *Trap5*× case. In other words, the amount of elapsed interlayer dwell time after deposition of the respective layers shown is identical for both cases. The *Trap10*× case still has nearly half of its interlayer dwell time to complete, yielding a lower overall temperature distribution prior to deposition of the subsequent layer.

A consequence of the longer dwell period for the *Trap10*× case is a lower initial layer-wise temperature distribution which results in mitigation of heat build-up. Since the interlayer dwell time is dynamic in the *Trap5*× and *Trap10*× cases, the heat build-up is more significant when compared with the *Trap43* and *Trap86* cases, where the interlayer dwell time was constant. Further, while the interlayer dwell time remained constant in the *Trap43* and *Trap86* cases, the deposition time decreased layer by layer due to the geometry of the part causing a reduction in layer-wise heat input, resulting in only moderate heat build-up. Again, due to the

thermal mass of the subsequent layers and the reduction in deposition at the beginning and end of the layers, the heat build-up is concentrated near the midpoint of the thin-walls.

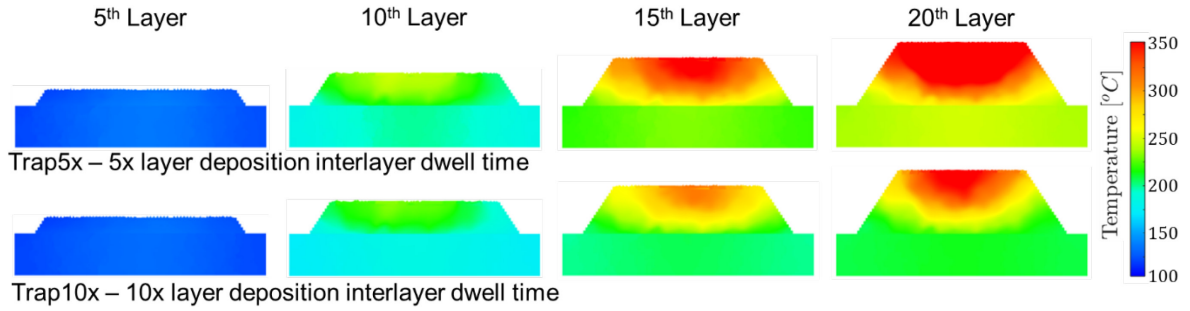

Figure 25: Simulated temperature distribution at the end of the interlayer dwell time after 5, 10, 15, and 20 layers have been deposited for cases *Trap5×* and *Trap10×* with interlayer dwell times corresponding to 5× and 10× the time taken to deposit the previous layer, respectively. Note the heat build-up in case *Trap5×* compared to case *Trap10×*.

4.4 Discussion

The two rectangle cases contained 15,408 nodes and the simulations converged in under 4.1 hours each. The four trapezoid cases contained 15,129 nodes and the simulation converged in under 3.5 hours each. The simulation time for the FE analysis with Simufact-Additive was 7.5 hours, which does not include the time to mesh and manually assemble the mesh in the Simufact software. The computation time, SMAPE, and RMSE for all six cases with respect to data from thermocouples TC1-TC4 are reported in Table 7. These results are calculated using the first experimental replicate, Experiment (a), as the reference for each case. The thermal history trends for thermocouples TC1, TC2, and TC4 are compared with the spectral graph predictions in Appendix B, where Figures 26, 27, 28, 29, 30, and 31 correspond to cases *Rect43*, *Rect86*, *Trap43*, *Trap86*, *Trap5×, and Trap10×*, respectively. For all cases, the predicted and experimentally observed temperature trends are in good agreement. The RMSE is less than 19 °C, with the SMAPE in the range of 1 – 5%.

The prediction errors are attributed to both the complex convective and radiative heat loss phenomena in the WAAM process as well as the modeling assumptions, such as temperature-independent material properties. Nevertheless, for a similar level of error, the spectral graph

method accurately predicted the experimental thermal trends at the thermocouple locations almost twice as fast as the commercial FE package.

Lastly, the simulation time of the spectral graph method is constrained by the number of nodes. The spectral graph method, the computational cost scales as $O(N^3)$, where N is the number of simulation nodes. In the current embodiment of the spectral graph method, since the node density is uniform, roughly 90% of the simulation nodes reside in the substrate, where thermal gradients are small for much of the build. A substantial improvement in both computation time and accuracy would accrue by lowering the node density where the thermal gradient is small, such as in the substrate.

Work is in progress to implement variable node density in the spectral graph method. Further, from the perspective of practical applications, in forthcoming work we are applying the spectral graph theory approach to predict the thermal history of a large part measuring 250 mm tall, with variations in welding energy, tool path, velocity, and interlayer dwell time. We will further correlate the influence of the predicted thermal history with microstructure observed in the finished part.

Table 7: Symmetric mean absolute percentage error (SMAPE) and root mean square error (RMSE), calculated by comparison between simulation results and experimental data, for all thermocouples and all experimental rectangle and trapezoid cases.

Case		Rect43	Rect86	Trap43	Trap86	Trap5×	Trap10×
Total nodes		15,408		15,129			
Computational hardware		AMD Ryzen 3970X CPU, @3.70 GHz with 128 GB RAM.					
Simulation run time [~hrs]		4.08	4.04	3.41	3.38	3.40	3.41
SMAPE [%]	Thermocouple TC1	2.11	5.31	1.06	2.08	3.65	2.00
	TC2	2.51	3.69	1.59	2.29	3.23	2.15
	TC3	3.27	1.67	2.59	3.42	1.54	3.16
	TC4	2.84	2.44	3.35	4.09	2.21	3.74
RMSE [°C]	TC1	7.82	19.08	3.91	6.73	13.18	6.49
	TC2	10.84	14.28	6.56	7.79	11.59	7.64
	TC3	13.19	5.64	10.32	10.91	6.19	12.14
	TC4	10.67	8.67	12.57	12.90	7.69	12.62

5. Conclusions

A current challenge in modeling the thermal history of large WAAM parts is the computational cost. In this work we developed, verified, and experimentally validated a mesh-free spectral graph theory method for rapid prediction of thermal history in WAAM parts. Specific outcomes are as follows.

- The approach was experimentally validated by processing multi-layer parts. Two different part shapes were processed under varying interlayer dwell time conditions, resulting in six unique experimental combinations. Each experiment was replicated once. Each part was 31.5 mm tall and consisted of 21 layers. During processing, the experimental thermal histories of each experimental case was recorded using five thermocouples embedded within the substrate.
- The error between the observed thermal history and those predicted using the spectral graph theory approach was quantified in terms of two statistical metrics, the symmetric mean absolute percent error (SMAPE) and root mean squared error (RMSE, °C). The spectral graph method predicted the temperature trends in approximately 4 hours, with SMAPE less-than 5% and most RMSE in the range of 4-11°C.
- The thermal history predictions from the spectral graph method were verified with a commercial FE-based thermal modeling package – Simufact Additive. The prediction results were compared for both part-level and layer-level thermal trends. For a level of prediction error similar to the graph theory approach, the commercial FE-based package required 7.5 hours.

The gain in computational efficiency without significantly sacrificing prediction accuracy afforded by the spectral graph method provides WAAM practitioners a physics-guided

alternative to the current expensive and cumbersome build-and-test empirical process parameter and toolpath optimization. For example, using the spectral graph method, the thermal history for a component can be rapidly simulated as a function of key process variables, such as welding power, tool path, and interlayer dwell time. Based on the insights obtained from these thermal simulations, the processing conditions can be optimized to avoid flaw formation, such as overheating. The thermal gradients and cooling rate predictions from the graph theory model could also potentially be used for estimating microstructure evolution.

Statements and Declarations

Funding

Authors Kevin D. Cole, Nicholas L. Piercy and Prahalada Rao, were supported by the U.S. Department of Energy (DoE), Office of Science, DE-SC0021136 (Program Officer: Timothy Fitzsimmons). The objective was the development of the graph theory approach for computational thermal modeling of the wire arc additive manufacturing process.

Author Prahalada Rao thanks the National Science Foundation (NSF) for funding his work under awards OIA-1929172, CMMI-1920245, CMMI-1739696, ECCS-2020246, PFI-TT 2044710, CMMI-1752069, CMMI-1719388. Using graph theory thermal modeling to improve part quality in metal additive manufacturing, such as laser powder bed fusion and directed energy deposition, was the major aspect of CMMI-1752069 (Program Officer: Kevin Chou) and PFI-TT 2044710 (Program Office: Samir Iqbal).

Authors Janmejay D. Kulkarni, Simhambhatla Suryakumar, and Aramuriparambil Santhosh Vishnu report that financial support was provided by the Indian Institute of Technology – Hyderabad.

The authors acknowledge the assistance of Alex Riensche and Reza Yavari for their help with the initial graph theory code, and Benjamin Bevans and Grant King for their support during code development.

Competing Interests

The authors have no competing interests to declare that are relevant to the content of this manuscript.

Availability of Data

The data sets generated for this study are available upon reasonable request to the corresponding author.

Code Availability

The spectral graph method described in the manuscript was carried out in MATLAB using custom code. FE verification was carried out using the commercial Simufact-Welding v7.1 software.

Ethics Approval

The authors declare that the manuscript is original, has not previously been published, and is not currently under consideration for publication elsewhere.

Consent to Participate

Not applicable.

Consent for Publication

Not applicable.

References

1. Spencer JD, Dickens PM, Wykes CM (1998) Rapid prototyping of metal parts by three-dimensional welding. Proc Inst Mech Eng B J Eng Manuf 212:175–182. https://doi.org/10.1243/0954405981515590

2. Kumar N, Bhavsar H, Mahesh PVS, et al (2022) Wire Arc Additive Manufacturing – A revolutionary method in additive manufacturing. Mater Chem Phys 285:126144. https://doi.org/10.1016/j.matchemphys.2022.126144

3. Williams SW, Martina F, Addison AC, et al (2016) Wire + Arc Additive Manufacturing. Materials Science and Technology 32:641–647. https://doi.org/10.1179/1743284715Y.0000000073

4. Christopher Holshouser, Clint Newell, Sid Palas, et al (2013) Out of Bounds Additive Manufacturing. Advanced Materials & Processes 171:171–173

5. Hassen AA, Noakes M, Nandwana P, et al (2020) Scaling Up metal additive manufacturing process to fabricate molds for composite manufacturing. Addit Manuf 32:101093. https://doi.org/10.1016/j.addma.2020.101093

6. Choo K, Friedrich B, Daugherty T, et al (2019) Heat retention modeling of large area additive manufacturing. Addit Manuf 28:325–332. https://doi.org/10.1016/j.addma.2019.04.014

7. Jin W, Zhang C, Jin S, et al (2020) Wire Arc Additive Manufacturing of Stainless Steels: A Review. Applied Sciences 10:1563. https://doi.org/10.3390/app10051563

8. Rodrigues TA, Duarte V, Avila JA, et al (2019) Wire and arc additive manufacturing of HSLA steel: Effect of thermal cycles on microstructure and mechanical properties. Addit Manuf 27:440–450. https://doi.org/10.1016/j.addma.2019.03.029

9. Suryakumar S, Karunakaran K, Chandrasekhar U, Somashekara M (2013) A study of the mechanical properties of objects built through weld-deposition. Proc Inst Mech Eng B J Eng Manuf 227:1138–1147. https://doi.org/10.1177/0954405413482122

10. Greer C, Nycz A, Noakes M, et al (2019) Introduction to the design rules for Metal Big Area Additive Manufacturing. Addit Manuf 27:159–166. https://doi.org/10.1016/j.addma.2019.02.016

11. Wu B, Pan Z, Ding D, et al (2018) A review of the wire arc additive manufacturing of metals: properties, defects and quality improvement. J Manuf Process 35:127–139. https://doi.org/10.1016/j.jmapro.2018.08.001

12. Riensche AR, Bevans BD, King G, et al (2024) Predicting meltpool depth and primary dendritic arm spacing in laser powder bed fusion additive manufacturing using physics-based machine learning. Mater Des 237:112540. https://doi.org/10.1016/j.matdes.2023.112540

13. Raghavan N, Simunovic S, Dehoff R, et al (2017) Localized melt-scan strategy for site specific control of grain size and primary dendrite arm spacing in electron beam additive manufacturing. Acta Mater 140:375–387. https://doi.org/10.1016/j.actamat.2017.08.038

14. Zhao H, Zhang G, Yin Z, Wu L (2012) Three-dimensional finite element analysis of thermal stress in single-pass multi-layer weld-based rapid prototyping. J Mater Process Technol 212:276–285. https://doi.org/10.1016/j.jmatprotec.2011.09.012

15. Huang H, Chen J, Carlson B, et al (2018) Stress and Distortion Simulation of Additive Manufacturing Process by High Performance Computing. In: Volume 6A: Materials and Fabrication. American Society of Mechanical Engineers

16. Michaleris P (2014) Modeling metal deposition in heat transfer analyses of additive manufacturing processes. Finite Elements in Analysis and Design 86:51–60. https://doi.org/10.1016/j.finel.2014.04.003

17. Oyama K, Diplas S, M'hamdi M, et al (2019) Heat source management in wire-arc additive manufacturing process for Al-Mg and Al-Si alloys. Addit Manuf 26:180–192. https://doi.org/10.1016/j.addma.2019.01.007

18. Peng H, Ghasri-Khouzani M, Gong S, et al (2018) Fast prediction of thermal distortion in metal powder bed fusion additive manufacturing: Part 1, a thermal circuit network model. Addit Manuf 22:852–868. https://doi.org/10.1016/j.addma.2018.05.023

19. Tangestani R, Sabiston T, Chakraborty A, et al (2021) An Efficient Track-Scale Model for Laser Powder Bed Fusion Additive Manufacturing: Part 1- Thermal Model. Front Mater 8:. https://doi.org/10.3389/fmats.2021.753040

20. Dugast F, Apostolou P, Fernandez A, et al (2021) Part-scale thermal process modeling for laser powder bed fusion with matrix-free method and GPU computing. Addit Manuf 37:101732. https://doi.org/10.1016/j.addma.2020.101732

21. Mozaffar M, Ndip-Agbor E, Lin S, et al (2019) Acceleration strategies for explicit finite element analysis of metal powder-based additive manufacturing processes using graphical processing units. Comput Mech 64:879–894. https://doi.org/10.1007/s00466-019-01685-4

22. Stockman T, Schneider JA, Walker B, Carpenter JS (2019) A 3D Finite Difference Thermal Model Tailored for Additive Manufacturing. JOM 71:1117–1126. https://doi.org/10.1007/s11837-019-03338-6

23. Ding D, Zhang S, Lu Q, et al (2021) The well-distributed volumetric heat source model for numerical simulation of wire arc additive manufacturing process. Mater Today Commun 27:102430. https://doi.org/10.1016/j.mtcomm.2021.102430

24. Nijhuis B, Geijselaers HJM, van den Boogaard AH (2021) Efficient thermal simulation of large-scale metal additive manufacturing using hot element addition. Comput Struct 245:106463. https://doi.org/10.1016/j.compstruc.2020.106463

25. Yang Y, Zhou X, Li Q, Ayas C (2021) A computationally efficient thermo-mechanical model for wire arc additive manufacturing. Addit Manuf 46:102090. https://doi.org/10.1016/j.addma.2021.102090

26. Kovšca D, Starman B, Klobčar D, et al (2023) Towards an automated framework for the finite element computational modelling of directed energy deposition. Finite Elements in Analysis and Design 221:103949. https://doi.org/10.1016/j.finel.2023.103949

27. Ding J, Colegrove P, Mehnen J, et al (2014) A computationally efficient finite element model of wire and arc additive manufacture. The International Journal of Advanced Manufacturing Technology 70:227–236. https://doi.org/10.1007/s00170-013-5261-x

28. Graf M, Hälsig A, Höfer K, et al (2018) Thermo-Mechanical Modelling of Wire-Arc Additive Manufacturing (WAAM) of Semi-Finished Products. Metals (Basel) 8:1009. https://doi.org/10.3390/met8121009

29. Ahmad SN, Manurung YH, Mat MF, et al (2020) FEM Simulation Procedure for Distortion and Residual Stress Analysis of Wire Arc Additive Manufacturing. IOP Conf Ser Mater Sci Eng 834:012083. https://doi.org/10.1088/1757-899X/834/1/012083

30. Yavari MR, Cole KD, Rao P (2019) Thermal Modeling in Metal Additive Manufacturing Using Graph Theory. J Manuf Sci Eng 141:. https://doi.org/10.1115/1.4043648

31. Yavari R, Williams R, Riensche A, et al (2021) Thermal modeling in metal additive manufacturing using graph theory – Application to laser powder bed fusion of a large volume impeller. Addit Manuf 41:101956. https://doi.org/10.1016/j.addma.2021.101956

32. Riensche A, Severson J, Yavari R, et al (2022) Thermal modeling of directed energy deposition additive manufacturing using graph theory. Rapid Prototyp J. https://doi.org/10.1108/RPJ-07-2021-0184

33. Cole KD, Riensche A, Rao PK (2022) Discrete Green's functions and spectral graph theory for computationally efficient thermal modeling. Int J Heat Mass Transf 183:. https://doi.org/10.1016/j.ijheatmasstransfer.2021.122112

34. Moylan S, Whitenton E, Lane B, Slotwinski J (2014) Infrared thermography for laser-based powder bed fusion additive manufacturing processes. pp 1191–1196

35. Panchagnula JS, Simhambhatla S (2018) Manufacture of complex thin-walled metallic objects using weld-deposition based additive manufacturing. Robot Comput Integr Manuf 49:194–203. https://doi.org/10.1016/j.rcim.2017.06.003

36. Li R, Xiong J, Lei Y (2019) Investigation on thermal stress evolution induced by wire and arc additive manufacturing for circular thin-walled parts. J Manuf Process 40:59–67. https://doi.org/10.1016/j.jmapro.2019.03.006

37. David SA, Babu SS, Vitek JM (2003) Welding: Solidification and microstructure. JOM 55:14–20. https://doi.org/10.1007/s11837-003-0134-7

38. Riensche A, Bevans BD, Smoqi Z, et al (2022) Feedforward control of thermal history in laser powder bed fusion: Toward physics-based optimization of processing parameters. Mater Des 224:111351. https://doi.org/10.1016/j.matdes.2022.111351

39. Ou W, Mukherjee T, Knapp GL, et al (2018) Fusion zone geometries, cooling rates and solidification parameters during wire arc additive manufacturing. Int J Heat Mass Transf 127:1084–1094. https://doi.org/10.1016/j.ijheatmasstransfer.2018.08.111

40. Goldak J, Chakravarti A, Bibby M (1984) A new finite element model for welding heat sources. Metallurgical Transactions B 15:299–305. https://doi.org/10.1007/BF02667333

41. Rosenthal D (1946) The Theory of Moving Sources of Heat and Its Application to Metal Treatments. J Fluids Eng 68:849–865. https://doi.org/10.1115/1.4018624

42. Cîndea L, Haţiegan C, Pop N, et al (2016) The influence of thermal field in the electric arc welding of X60 carbon steel components in the CO2 environment. Appl Therm Eng 103:1164–1175. https://doi.org/10.1016/j.applthermaleng.2016.05.004

43. Gery D, Long H, Maropoulos P (2005) Effects of welding speed, energy input and heat source distribution on temperature variations in butt joint welding. J Mater Process Technol 167:393–401. https://doi.org/10.1016/j.jmatprotec.2005.06.018

44. Chergui A, Beraud N, Vignat F, Villeneuve F (2021) Finite Element Modeling and Validation of Metal Deposition in Wire Arc Additive Manufacturing. pp 61–66

45. Flint TF, Francis JA, Smith MC, Balakrishnan J (2017) Extension of the double-ellipsoidal heat source model to narrow-groove and keyhole weld configurations. J Mater Process Technol 246:123–135. https://doi.org/10.1016/j.jmatprotec.2017.02.002

46. Montevecchi F, Venturini G, Scippa A, Campatelli G (2016) Finite Element Modelling of Wire-arc-additive-manufacturing Process. Procedia CIRP 55:109–114. https://doi.org/10.1016/j.procir.2016.08.024

47. Oliveira AVS, Avrit A, Gradeck M (2022) Thermocouple response time estimation and temperature signal correction for an accurate heat flux calculation in inverse heat conduction problems. Int J Heat Mass Transf 185:. https://doi.org/10.1016/j.ijheatmasstransfer.2021.122398

48. Chen Q, Liang X, Hayduke D, et al (2019) An inherent strain based multiscale modeling framework for simulating part-scale residual deformation for direct metal laser sintering. Addit Manuf 28:406–418. https://doi.org/10.1016/j.addma.2019.05.021

49. Hackenhaar W, Mazzaferro JAE, Montevecchi F, Campatelli G (2020) An experimental-numerical study of active cooling in wire arc additive manufacturing. J Manuf Process 52:58–65. https://doi.org/10.1016/j.jmapro.2020.01.051

50. Zhou J, Barrett RA, Leen SB (2022) Three-dimensional finite element modelling for additive manufacturing of Ti-6Al-4V components: Effect of scanning strategies on temperature history and residual stress. Journal of Advanced Joining Processes 5:100106. https://doi.org/10.1016/j.jajp.2022.100106

51. Yang Q, Zhang P, Cheng L, et al (2016) Finite element modeling and validation of thermomechanical behavior of Ti-6Al-4V in directed energy deposition additive manufacturing. Addit Manuf 12:169–177. https://doi.org/10.1016/j.addma.2016.06.012

Appendix A

This appendix contains tabulated root mean square (RMS) deviation values for the replicate experiments conducted within the study. Since each experiment yields a primary and a replicate thin-wall, the variation between the collected thermal data is quantified in terms of RMS. The RMS for most of the cases is within 15 °C, with a maximum deviation of 17 °C, and a minimum of 3 °C. The variation observed between replicate experiments is attributed to environmental conditions and fleeting inconsistencies in the manufacture of the substrates, placement of thermocouples, kinematic errors from the machinery, and start-stop location of each thin-wall.

The RMS deviation is calculated as:

$$RMS = \sqrt{\sum_{i}^{n} \frac{(T_{a,t_i} - T_{b,t_i})^2}{n}} \tag{14}$$

where n is the number of recorded time steps and T_a, T_b are the recorded thermocouple temperatures at time t_i for the replicate experiments 'a' and 'b', respectively. In Table 8, TC1 represents thermocouple 1, and so on.

Table 8: Variation between replicate experiments 'a' and 'b' for each geometry and interlayer dwell time case.

Thin-wall	Root Mean Square (RMS) Deviation [°C]			
	TC1	TC2	TC3	TC4
Rect43	14.52	13.26	10.42	12.67
Rect86	17.00	10.11	9.91	10.24
Trap43	2.86	3.29	3.80	5.27
Trap86	13.20	12.10	11.73	12.46
Trap5×	12.60	11.75	9.91	12.58
Trap10×	12.83	16.12	11.16	11.01

Appendix B

This appendix contains data from thermocouples TC1, TC2, and TC4 plotted alongside the spectral graph simulations corresponding to those thermocouple locations in the substrate. The behaviors exhibited here are similar to those of thermocouple 3 (TC3), which have been discussed in Section 4 of the paper. For the rectangular cases, the *Rect43* and *Rect86* simulation results are graphically compared with the experimental thermocouple data in Figure 26 and Figure 27, respectively. For the trapezoidal cases, the *Trap43* and *Trap86* simulation results are graphically compared with the thermocouple data in Figure 28 and Figure 29, respectively. Finally, the simulation results for the *Trap5*× and *Trap10*× cases are compared with the thermocouple data in Figure 30 and Figure 31, respectively. The calculated SMAPE and RMSE values are reported in Table 7 for all cases.

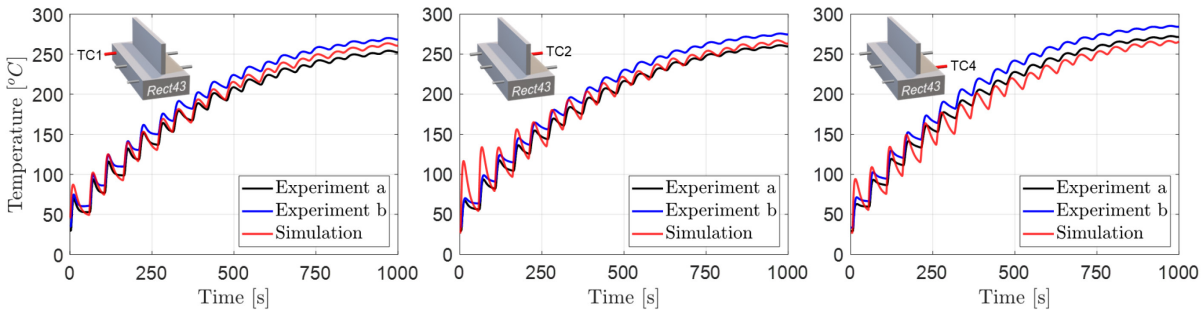

Figure 26: Thermal history comparison between experimental data and the spectral graph thermal simulation at thermocouple locations TC1, TC2, and TC 4 for the rectangular thin-wall case *Rect43* with a constant 43 second interlayer dwell time ($t_d = 43$ s).

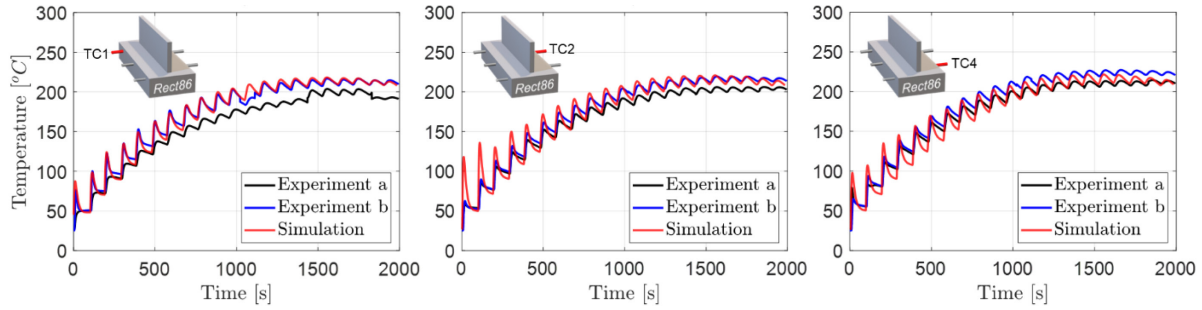

Figure 27: Thermal history comparison between experimental data and the spectral graph thermal simulation at thermocouple locations TC1, TC2, and TC4 for the rectangular thin-wall case *Rect86* with a constant 86 second interlayer dwell time ($t_d = 86$ s).

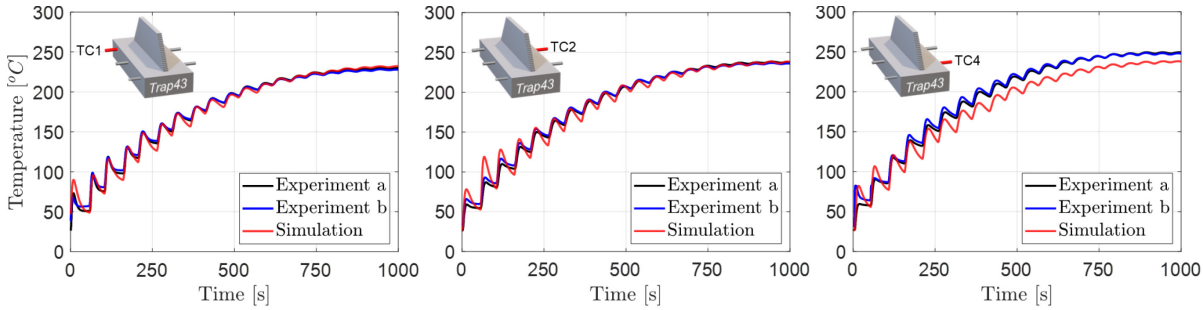

Figure 28: Thermal history comparison between experimental data and the spectral graph thermal simulation at thermocouple locations TC1, TC2, and TC4 for the trapezoidal thin-wall case *Trap43* with a constant 43 second interlayer dwell time ($t_d = 43$ s).

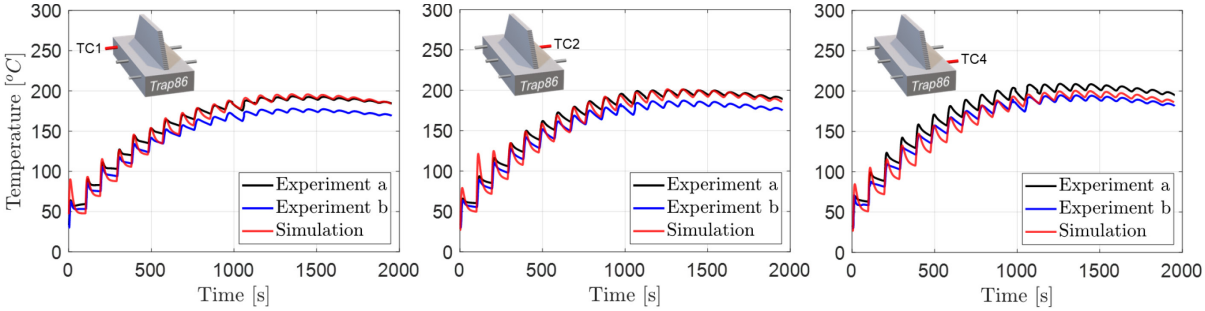

Figure 29: Thermal history comparison between experimental data and the spectral graph thermal simulation at thermocouple locations TC1, TC2, and TC4 for the trapezoidal thin-wall case *Trap86* with a constant 86 second interlayer dwell time ($t_d = 86$ s).

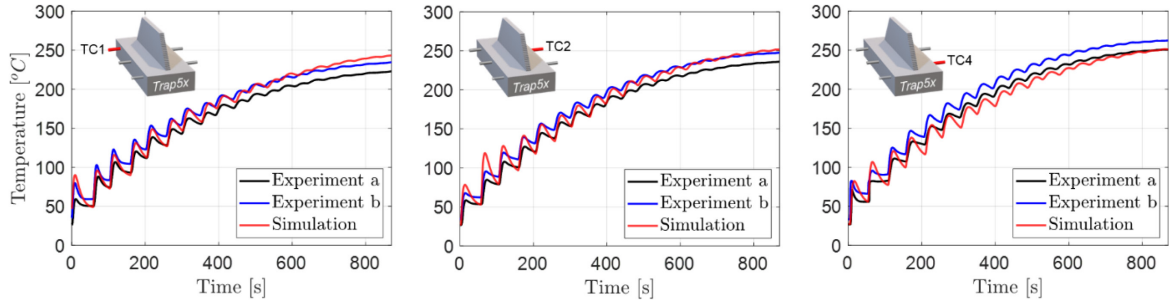

Figure 30: Thermal history comparison between experimental data and the spectral graph thermal simulation at thermocouple locations TC1, TC2, and TC4 for the trapezoidal thin-wall case *Trap5×* with a non-constant interlayer dwell time equal to 5× the time taken to deposit the previous layer ($t_d = 5 \times t_{i-1}$).

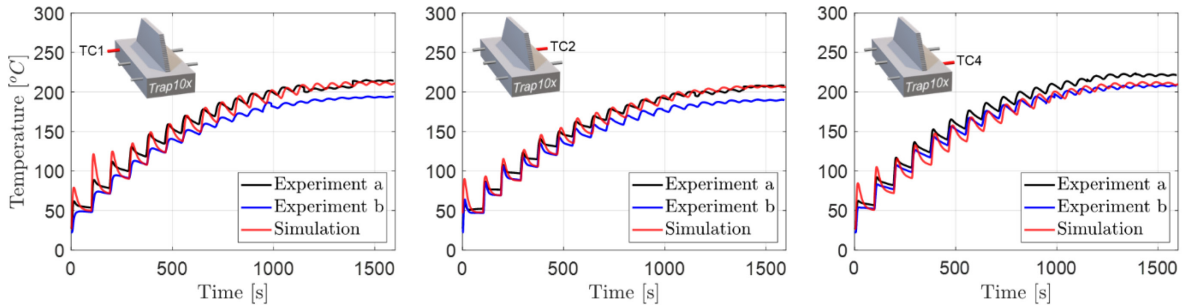

Figure 31: Thermal history comparison between experimental data and the spectral graph thermal simulation at thermocouple locations TC1, TC2, and TC4 for the trapezoidal thin-wall case *Trap10×* with a non-constant interlayer dwell time equal to 10× the time taken to deposit the previous layer ($t_d = 10 \times t_{i-1}$).

A general observation is that the simulated temperature trends increasingly agree with the experimental data as each build progresses from start to finish. In the early stages of the build, the simulated trends peak slightly higher than the experimental data suggests, however, this is expected in a physical sense from the delays introduced by thermocouple time constants, which are described by Oliveira et al. [47] in their work. Late in the build, the same rapid temperature rise is not expected as the heat source is further from the thermocouple location. As deposition continues and the build plane moves further from the thermocouples, the time delay contribution from the thermocouple time constant decreases.

Appendix C

This appendix discusses filtering of the simulated temperature history results prior to comparison with the experimentally collected temperature data. This filtering compensates for the slow response time associated with the thermocouples used in the study. Both the spectral graph method and the finite element method (Simufact-Welding) simulate temperature history at physical locations within the part without delay. Hence, prior to comparing the simulated temperature responses to those captured by the experimental thermocouples, filtering of the simulated data is required to impose the effect of the estimated response time of the thermocouples on the simulated temperatures.

The 5 mm diameter, substrate-embedded thermocouples used in this study were K-type, installed in a metal sheath with an air gap between the thermocouple bead and the sheath. These are ungrounded thermocouples, which are known to have a time-constant which dampens rapid variations in the recorded thermocouple response. For a 5 mm diameter ungrounded K-type thermocouple, the time-constant is estimated to be 2.25 s, however, the time-constant is defined as the time taken for the sensor to reach 63.2% of the bulk temperature reading. On the other hand, the thermocouple response time, τ^*, is defined as the time taken for the sensor to reach 99.3% of the bulk temperature reading, which occurs after five time-constants. In other words, the response time τ^* is the time required for the thermocouple to be considered in thermal equilibrium with the substrate and, in this study, is calculated to be $\tau^* = 5 \times 2.25$ s = 11.25 s.

The dampening effect of the response time is proportional to the rate and intensity of any given temperature rise where fast, sharp increases in temperature are dampened more than slow, moderate temperature increases. In a study by Oliveira et al. [47] the dampening effect of ungrounded, embedded thermocouples was studied for fast thermal transient situations which are similar to weld deposition during the beginning layers of the build. In their study,

temperatures recorded by the ungrounded (slow) thermocouples were substantially dampened when compared with exposed (fast) thermocouples.

The relationship between the simulated temperatures and the filtered temperatures is given by:

$$T_f^k - T_{SG}^k = \tau^* \frac{dT_f^k}{dt^k} \tag{15}$$

Here, T_{SG}^k and T_f^k are the simulated spectral graph (SG) and filtered (f) temperatures, respectively, at time instant k. Solving Equation (15), the filtered temperature at time instant k, is given by:

$$T_f^k = T_{SG}^k + \left(T_f^{k-1} - T_{SG}^k\right) e^{\frac{-\Delta t}{\tau^*}} \tag{16}$$

Here, Δt is the elapsed time between time instant $k-1$ and time instant k. The filtered simulation temperature T_f accounts for the response time of the experimental thermocouples, which supports the comparison between simulated and experimentally collected temperature histories.

Hence, prior to comparing the spectral graph simulated temperature histories with the experimental thermocouple data, the simulated data was filtered per Eqn. (15)-(16) with response time τ^* = 11.25 s.